Reports on Progress in Physics





PAPER • OPEN ACCESS

Divergence beneath the Brillouin sphere and the phenomenology of prediction error in spherical harmonic series approximations of the gravitational field

To cite this article: M Bevis et al 2024 Rep. Prog. Phys. 87 078301

View the article online for updates and enhancements.

You may also like

- Metal-insulator transitions in pyrochlore oxides
 Vashinari Tokura, Vukitoshi Motome and
- Yoshinori Tokura, Yukitoshi Motome and Kentaro Ueda
- Beyond Kitaev physics in strong spin-orbit coupled magnets
 Ioannis Rousochatzakis, Natalia B
 Perkins, Qiang Luo et al.
- 70 years of hyperon spectroscopy: a review of strange, baryons, and the spectrum of charmed and bottom baryons Volker Crede and John Yelton



Rep. Prog. Phys. 87 (2024) 078301 (31pp)

https://doi.org/10.1088/1361-6633/ad44d5

Divergence beneath the Brillouin sphere and the phenomenology of prediction error in spherical harmonic series approximations of the gravitational field

M Bevis^{1,*}, C Ogle², O Costin², C Jekeli¹, R D Costin², J Guo¹, J Fowler², G V Dunne³, C K Shum¹ and K Snow¹

E-mail: mbevis@osu.edu

Received 25 August 2023, revised 20 March 2024 Accepted for publication 29 April 2024 Published 20 June 2024

Corresponding editor: Mrs Natasha Leeper



Abstract

The Brillouin sphere is defined as the smallest sphere, centered at the origin of the geocentric coordinate system, that incorporates all the condensed matter composing the planet. The Brillouin sphere touches the Earth at a single point, and the radial line that begins at the origin and passes through that point is called the singular radial line. For about 60 years there has been a persistent anxiety about whether or not a spherical harmonic (SH) expansion of the external gravitational potential, V, will converge beneath the Brillouin sphere. Recently, it was proven that the probability of such convergence is zero. One of these proofs provided an asymptotic relation, called Costin's formula, for the upper bound, E_N , on the absolute value of the prediction error, e_N , of a SH series model, $V_N(\theta, \lambda, r)$, truncated at some maximum degree, $N = n_{\text{max}}$. When the SH series is restricted to (or projected onto) a particular radial line, it reduces to a Taylor series (TS) in 1/r. Costin's formula is $E_N \simeq BN^{-b}(R/r)^N$, where R is the radius of the Brillouin sphere. This formula depends on two positive parameters: b, which controls the decay of error amplitude as a function of N when r is fixed, and a scale factor B. We show here that Costin's formula derives from a similar asymptotic relation for the upper bound, A_n on the absolute value of the TS coefficients, a_n , for the same radial line. This formula, $A_n \simeq K n^{-k}$, depends on degree, n, and two positive parameters, k and K, that are analogous to b and B. We use synthetic planets, for which we can compute the potential, V, and also the radial component of gravitational acceleration, $g_r = \partial V/\partial r$, to hundreds of significant digits, to validate both of these asymptotic formulas. Let superscript V refer to asymptotic parameters

Original Content from this work may be used under the terms of the Creative Commons Attribution 4.0 licence. Any further distribution of this work must maintain attribution to the author(s) and the title of the work, journal citation and DOI.

¹ Division of Geodetic Science, School of Earth Sciences, The Ohio State University, Columbus, OH, United States of America

² Department of Mathematics, The Ohio State University, Columbus, OH, United States of America

³ Department of Physics, University of Connecticut, Storrs, CT, United States of America

^{*} Author to whom any correspondence should be addressed.

associated with the coefficients and prediction errors for gravitational potential, and superscript g to the coefficients and predictions errors associated with g_r . For polyhedral planets of uniform density we show that $b^V = k^V = 7/2$ and $b^g = k^g = 5/2$ almost everywhere. We show that the frequency of oscillation (around zero) of the TS coefficients and the series prediction errors, for a given radial line, is controlled by the geocentric angle, α , between that radial line and the singular radial line. We also derive useful identities connecting K^V, B^V, K^g , and B^g . These identities are expressed in terms of quotients of the various scale factors. The only other quantities involved in these identities are α and R. The phenomenology of 'series divergence' and prediction error (when r < R) can be described as a function of the truncation degree, N, or the depth, d, beneath the Brillouin sphere. For a fixed $r \le R$, as N increases from very low values, the upper error bound E_N shrinks until it reaches its minimum (best) value when N reaches some particular or optimum value, N_{opt} . When $N > N_{\text{opt}}$, prediction error grows as Ncontinues to increase. Eventually, when $N \gg N_{\rm opt}$, prediction errors increase exponentially with rising N. If we fix the value of N and allow R/r to vary, then we find that prediction error in free space beneath the Brillouin sphere increases exponentially with depth, d, beneath the Brillouin sphere. Because $b^g = b^V - 1$ everywhere, divergence driven prediction error intensifies more rapidly for g_r than for V, both in terms of its dependence on N and d. If we fix both N and d, and focus on the 'lateral' variations in prediction error, we observe that divergence and prediction error tend to increase (as does B) as we approach high-amplitude topography.

Keywords: spherical harmonic expansion, divergence, gravitational potential, asymptotic

1. Introduction

The Brillouin sphere is defined as the smallest sphere, centered at the center of the Earth (or other planet), that incorporates all the condensed matter composing the planet. It is possible to define a Brillouin ellipsoid similarly, by using an oblate ellipsoid of rotation instead of a sphere. Either Brillouin surface will touch the ground at a single point. For Earth's Brillouin sphere, that point is the summit of Mt. Chimborazo in Ecuador, which is the surface point most distant from the geocenter, by virtue of that mountain's position near the crest of the equatorial bulge. In contrast, the Brillouin ellipsoid touches the Earth at the summit of Mt. Everest, which has the greatest ellipsoidal height of any point on the Earth. In this work, we discuss spherical harmonic (SH) representations of the gravitational field. In this context, we can define the geocenter (or the center of some other planet of interest) as the origin of the coordinate system used to define the SHs. Ideally, the origin coincides with the planet's center of mass. In practice, the origin will lie very close to the center of mass. In this treatment, we will neglect temporal variation of the gravitational field and the gravitational impact of Earth's atmosphere.

In 'free space' devoid of mass, gravitational potential V obeys Laplace's equation $\nabla^2 V = 0$. In the eighteenth century, Laplace, building on the work of Legendre, showed that it was possible to solve this equation in spherical coordinates using SH functions. By the early twentieth century, physicists, geodesists and mathematicians routinely assumed that the gravitational potential $V(r, \theta, \lambda)$ outside of the Earth could be represented using a SH expansion (SHE) of the form

$$V = \frac{GM}{R} \sum_{n=0}^{\infty} \left(\frac{R}{r}\right)^{n+1} \sum_{m=0}^{n} \left(c_{nm} \cos m\lambda + s_{nm} \sin m\lambda\right) P_n^m \left(\cos \theta\right),$$

where G is the universal constant of gravitation, M is the mass of the Earth, θ and λ are colatitude and longitude, ris the radial coordinate, and R is the radius of some reference sphere. In recent decades, R is usually equated with the semi-major axis length of a reference ellipsoid that approximates sea level. The summation indices n and m are called the degree and order of the expansion, respectively, and the terms c_{nm} and s_{nm} are its coefficients. The P_n^m are the associated Legendre functions (also called the associated Legendre polynomials); these reduce to the Legendre polynomials P_n when m = 0. That is, $P_n^0 = P_n$ for any value of n. When m = 0 then $\sin m\lambda = 0$, causing this term to disappear along with its coefficient. Thus for each degree n there are a total of 2n + 1 coefficients. Mathematicians should note that geodesists routinely call *n* the degree of the SHE, even though the exponent of R/ris n+1.

The degree-1 terms in equation (1) express the displacement of the origin of the coordinate system from the center of mass of the planet. If the origin exactly coincides with the center of mass, all the degree-1 coefficients are zero, and the corresponding terms vanish from the expansion.

Obviously, equation (1) describes an infinite series. In practice, numerical models of the gravitational field are truncated at some maximum degree N, and the result is the finite SH series

$$V = \frac{GM}{R} \sum_{n=0}^{N} \left(\frac{R}{r}\right)^{n+1} \sum_{m=0}^{n} \left(c_{nm} \cos m\lambda + s_{nm} \sin m\lambda\right) P_n^m \left(\cos \theta\right). \tag{2}$$

The larger the value of *N*, the better the spatial resolution of this model. Mathematicians refer to equation (2) as a SH polynomial. But most geodesists and geophysicists refer to it as a SH series, without adding the qualifier 'finite' or 'truncated.'

This is unfortunate since mathematicians normally interpret the word *series* to imply an infinite series.

The gravitational acceleration vector, \mathbf{g} , is obtained from V by differentiation:

$$\mathbf{g} = \nabla V,\tag{3}$$

where ∇ is the gradient operator (section 7.1).

The P_n^m in equations (1) and (2) can be normalized in a variety of ways—e.g. Guo (2023)—but normalization is not really relevant to this study, nor would it affect our findings, so we will not discuss it here.

It is worth noting that there are two different sign conventions in use for the potential function V. For physicists and most geophysicists, the gravitational potential V is negative, consistent with the notion that the Earth sits in a potential well of its own making. In this case, the gravitational acceleration vector $\mathbf{g} = -\nabla V$. But nearly all geodesists define V to be positive, in which case $\mathbf{g} = \nabla V$. In the case of a spherical Earth model, in which density is constant or spherically symmetric, most physicists define V = -GM/r whereas most geodesists define V = GM/r. But both groups agree as to the sign and magnitude of gravitational force and acceleration.

2. The problem of divergence

By the early 1960s, it was widely understood that the SHE of V, equation (1), is guaranteed to converge for any value of rgreater than the radius, R_B , of the Brillouin sphere (Kellogg 1929), but there was no such guarantee inside of that sphere. Moritz (1961) argued that the expansion of the actual potential V should be considered divergent at the surface of the Earth. Heiskanen and Moritz (1967) amended that position when they stated the expansion will usually be divergent for any $r < R_B$. This brought into question the utility of SH series for approximating the external gravitational field anywhere near the surface of the Earth. Krarup (1969) emphasized the extreme instability of the property of convergence (when r < R_B), noting that if the expansion of some external potential V was convergent down to the planet's surface, the tiniest perturbation, even that caused by the introduction of a single grain of sand, could render the expansion divergent. But Krarup (1969) also argued that a generalization of Runge's theorem (now called the Runge-Krarup theorem by geodesists) implies that non-convergence is a non-problem in practice. As Moritz (1980) put it

... let us for brevity introduce the name 'convergent potential' for an external potential whose spherical harmonic expansion is convergent on or outside the Earth's surface. Then the theorem by Runge-Krarup states that the set of 'convergent potentials' is dense within the set of all external potentials, just as the rationals are dense within the set of real numbers.

The analogy being drawn is that every irrational number can be approximated with arbitrary accuracy by a rational number, because the rational numbers are dense within the set of real numbers. Given that any physical measurement has limited precision, the question as to whether the quantity being measured, say a distance, should be represented by a rational or an irrational number is moot and physically meaningless. Within the range of uncertainty of the measurement, there would always be 'infinitely many rational and infinitely many irrational numbers, all of them perfectly respectable and equally suited for the office of numerically representing the distance under consideration.' Moritz used this analogy to explain that, in the space of all potentials, there would be infinitely many convergent potentials and infinitely many divergent potentials located arbitrarily close to the actual potential of the Earth, and therefore, in practice, there will always be a convergent potential that can approximate the actual exterior potential of the Earth to any desired degree of accuracy.

Hofmann-Wellenhof and Moritz (2006) expressed what was still a widely held opinion a quarter of a century later: that the spherical harmonic series of the actual potential V of the Earth can be divergent or convergent at the surface of the Earth, and 'theoretically, this makes the use of a harmonic expansion of V at the Earth's surface somewhat difficult; practically, it is always safe to regard it as convergent.'

Despite Krarup's and Moritz's assurances that non-convergence was a non-problem in practice, geodesists engaged in constructing global gravitational models using SH series, equation (2), occasionally reported numerical experiments that seemed to manifest divergence, e.g. Jekeli (1983). From the early 1980s to the present day, those building such models have tended to improve their resolution, and better exploit growing collections of terrestrial and space-based measurements of gravitation and gravity, by increasing the truncation degree N of their models. If the underlying SHE of V is diverging, the higher the value of N, the more likely that the finite SH series will manifest or illuminate this divergent behavior. Jekeli (1983) referred to such non-convergent behavior as 'series divergence,' whereas Bucha $et\ al\ (2019)$ described it as 'the divergence effect.'

Hirt and Kuhn (2017) investigated the 'divergence issue' using a set of SH series approximations for the external potential of the Moon. In these numerical experiments, the gravity field generated by lunar topography was forward-modeled in spherical harmonics using numerical integration techniques, at various heights and different levels of resolution. In successive experiments, N was increased from 90 to 2160. They found that the spherical harmonic gravity field generated from degree-180 topography was convergent everywhere in free space, but when the topographic mass model was complete through degree 360, divergence started to affect very high degree gravity signals over regions deep inside the Brillouin sphere. For topography and gravity models with N = 2160, divergence was so severe (with several 1000 mGal amplitudes) it prohibited accurate gravity modeling over most of the topography. This result is consistent with previous suggestions that divergence is more likely to occur the higher the truncation degree N, the more extreme the planetary topography, and the deeper the evaluation point lies beneath the Brillouin sphere (Wang 1997, Lowes and Winch 2012, Hu and Jekeli 2015).

The increasing frequency and persuasiveness of published claims concerning series divergence, and our own numerical experiments conducted with entirely synthetic planets, prompted Ogle et al (2021) and Costin et al (2022) to revisit the question of whether or not a SHE of V would converge. Both studies used purely analytical approaches. Ogle et al (2021) used the methods of differential topology, and Costin et al (2022) used modern asymptotic approximation theory. They proved that, for any realistic planet with topography, the probability that a SHE for V will converge in free space beneath the Brillouin surface is zero. This may seem surprising given the Runge-Krarup theorem, which implies that there are an infinite number of convergent potentials, as well as an infinite number of divergent potentials, arbitrarily close to a given external potential. The apparent contradiction is resolved when we understand:

- (i) For each convergent potential in any small neighborhood of the space of all external potentials, there are infinitely many more divergent potentials.
- (ii) The Runge-Krarup theorem is an existence theorem. It does not provide a method for finding or constructing a convergent potential. No such method has been found.

Very loosely speaking, any procedure for evaluating the coefficients of the expansion which cannot steer the result towards a convergent potential is going to arrive at a divergent potential, because the latter are infinitely more common than the former.

We can re-purpose Moritz's analogy of rational versus irrational numbers in order to illustrate a parallel idea. Even though there are infinitely many rational numbers in any segment of the real line, no matter how small that interval is, for each rational number in that segment there are infinitely many more irrational numbers. Therefore, if we randomly pick a point (i.e. a real number) on the real line, the probability that it will be a rational number is zero.

For further reading on the topic of convergence/divergence we recommend Ecker (1972), Kholshevnikov (1977), Sjöberg (1980), Sansò and Sideris (2013), Fukushima (2020) and the references therein.

3. The structure and goals of this study

Since there has been considerable confusion concerning the divergence of the SHE, and the results of Ogle *et al* (2021) and Costin *et al* (2022) may be viewed as somewhat abstract, in this current paper we aim to present both analytical and numerical results which demonstrate clearly how and why the SHE is divergent, and illustrate the practical numerical consequences of this divergence.

In this work we will utilize the analytical framework of Costin *et al* (2022). The analysis of Ogle *et al* (2021) is also of interest because the two proofs arrive at similar conclusions concerning the presence of divergence beneath the

Brillouin sphere, using remarkably different methodologies. Furthermore, the Ogle *et al* (2021) proof is based on a more minimal set of assumptions concerning the continuity of the planet. But the analysis of Costin *et al* (2022) is of greater importance in that it establishes the necessary conditions for convergence beneath the Brillouin sphere (which has zero probability), and because it provides us with a powerful framework for analyzing the phenomenology of the series approximation error driven by divergence. The main goals of this work are (1) to demonstrate that some key findings of Costin *et al* (2022) can be tested using numerical experiments, and that these tests are always passed, (2) to extend the original theory, and (3) to elucidate the phenomenology of divergence-driven series prediction error.

The greatest impediment to assessing the prediction errors produced by SH series approximations for the Earth's external potential V is that we do not know the exact or true value to compare with. For this reason we will focus on the gravitational potential of artificial or synthetic planets, which we can compute anywhere in free space to hundreds of significant digits, allowing a direct assessment of series prediction error, both as a function of spatial position (especially with respect to depth below the Brillouin sphere) and as a function of the series truncation degree N.

4. Some preliminaries

One way of representing a SH series (normalized so that GM/R=1), that emphasizes the sum on degree, n, is

$$V_N = \sum_{n=0}^{N} (R/r)^{n+1} Y_n(\theta, \lambda), \qquad (4)$$

where

$$Y_n(\theta,\lambda) = \sum_{m=0}^{n} (c_{nm}\cos m\lambda + s_{nm}\sin m\lambda) P_n^m(\cos\theta). \quad (5$$

In general, the right-hand side of equation (5) has a total of 2n + 1 non-zero terms.

Suppose we wish to evaluate the SH series on a radial line A passing through points with angular coordinates (θ_A, λ_A) . Restricting $Y_n(\theta, \lambda)$ to $Y_n(\theta_A, \lambda_A)$ reduces it to a constant a_n where, for any n,

$$a_n = \sum_{m=0}^{n} (c_{nm} \cos m\lambda_A + s_{nm} \sin m\lambda_A) P_n^m (\cos \theta_A), \quad (6)$$

so, on this same axis A, equation (4) reduces to

$$V_N^A = \sum_{n=0}^N a_n (R/r)^{n+1} = a_0 (R/r) + a_1 (R/r)^2 + a_2 (R/r)^3 + \dots + a_N (R/r)^{N+1}.$$
 (7)

We can equate this expression with a Taylor polynomial in R/r.

The Taylor series (TS), or Taylor expansion, of a real or complex function f(z) that is infinitely differentiable at z = a is the power series

$$f(z) = \sum_{k=0}^{\infty} \frac{f^{(k)}(a)}{k!} (z - a)^k,$$
 (8)

where $f^{(k)}(a)$ is the kth derivative of f(z) evaluated at z = a, $f^{(0)}(a) = f(a)$ and 0! = 1. If a = 0, then the Taylor expansion reduces to

$$f(z) = \sum_{k=0}^{\infty} \frac{f^{(k)}(0)}{k!} z^k$$
 (9)

or

$$f(z) = \sum_{k=0}^{\infty} b_k z^k = b_0 + b_1 z + b_2 z^2 + \dots$$
 (10)

where $b_k = f^{(k)}(0)/k!$. In the event that we truncate the Taylor expansion at k = M, we obtain the Taylor polynomial

$$f(z) = \sum_{k=0}^{M} b_k z^k = b_0 + b_1 z + b_2 z^2 + \dots + b_M z^M.$$
 (11)

We can associate equation (7) with this Taylor polynomial by making the substitution $R/r \rightarrow z$ in equation (7). This means that equation (7) is rewritten as

$$V_N^A = \sum_{n=0}^N a_n z^{n+1} = a_0 z + a_1 z^2 + a_2 z^3 + \dots + a_N z^{N+1}. \quad (12)$$

The reader should not confuse the variable z with the geocentric Cartesian coordinate, which we represent with Z. We sometimes use z to indicate any real or complex variable, as in equation (11), and sometimes to mean the quotient R/r, as in equation (12). The particular usage should be obvious from the context.

There is another potential source of confusion for the unwary, since mathematicians refer to k as the degree of the Taylor polynomial (equation (11)), whereas geodesists refer to k as the degree of the SHE (equation (1)), and this is the same k that appears in equation (12).

In the context of our gravitational problem, z=0 corresponds to $r=\infty$. Because $V \to 0$ as $r \to \infty$, there is no constant term of the right-hand side of equation (7) or equation (12). Therefore, to equate f(z) in equation (11) with V_N^A in equation (12) we must set the constant $b_0=0$, so that the first term on the right-hand side of equation (11) vanishes, and set $b_n=a_{n-1}$ for n>0, and set M=N+1.

With these qualifications in mind, we conclude that the spatial restriction (or projection) of a SH series onto a specific radial line reduces the SH series to a truncated TS (or Taylor polynomial) in R/r. Similarly, the divergence of the SHE in free space anywhere beneath the Brillouin sphere will manifest as the divergence (in free space) of the TS on the radial line, if $r < R_{\rm B}$, no matter the choice of radial line.

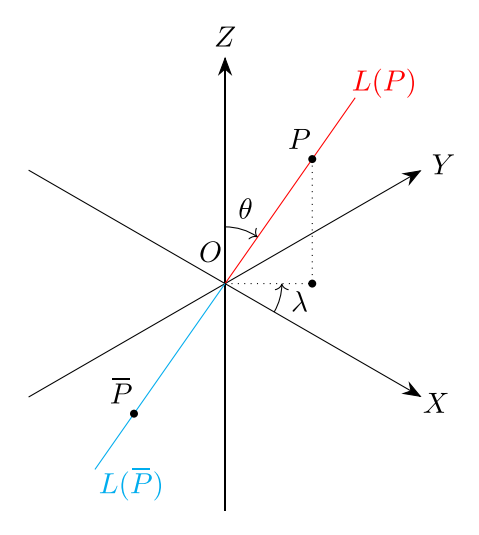


Figure 1. A radial line L(P) that passes through some point P (that is not coincident with the origin O) is entirely determined by the geocentric colatitude, θ , and longitude, λ , of P. The complementary radial line $L(\bar{P})$ contains the point \bar{P} which is antipodal to point P.

S is the singular radial line

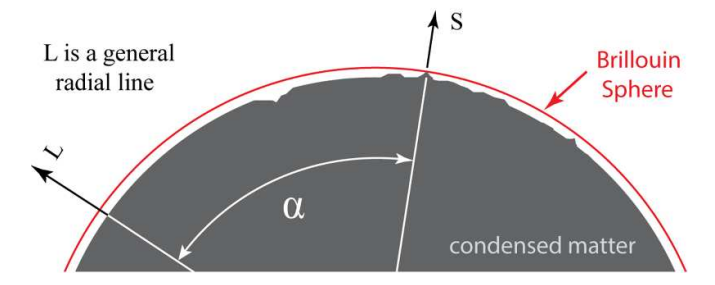


Figure 2. A section through the center of the planet containing the singular radial line S and an arbitrary radial line of interest, L. The geocentric angle between S and L is α . In the case of the Earth, S would pass through Mt. Chimborazo in Ecuador.

We conclude this section by introducing some useful terminology associated with radial lines. Radial lines are half-lines that begin at the origin, O, of the geocentric coordinate system, and extend to infinity (figure 1). All the points on a radial line (excluding the origin) have the same angular coordinates (θ, λ) . Thus we can specify a radial line L(P) by providing the coordinates of any point P on that line. The complementary radial line $L(\bar{P})$ passes through a point \bar{P} which is antipodal to point P. The union of L(P) and $L(\bar{P})$ is a line or axis that passes through P, O and \bar{P} .

If a radial line passes through the single point of contact between the surface of the planet and its Brillouin sphere, we refer to this radial line as the *singular radial line* (figure 2). The Earth has a singular radial line, and the same would almost certainly be true for any rocky planet or moon. A singular radial line and its complementary radial line jointly compose a *singular axis*. In section 7, we will see that a very important control on divergence and series prediction error along any radial line L is the geocentric angle α between L and the singular radial line S (figure 2).

5. An asymptotic expression for the bound on series prediction error

5.1. The Costin formula

A SH series is a function of co-latitude, θ , longitude, λ , and r. But if we restrict the SH series to specific values of θ and λ , then it depends on r alone. Indeed, it reduces to a Taylor polynomial in R/r where $R=R^{\rm ref}$ is the radius of the reference sphere.

Suppose, at some point P, the exact value of potential is V, and the finite TS approximation is V_N , where $N = n_{\text{max}}$ is the truncation degree. Then the prediction error is $e_N = V_N - V$, and the relative prediction error is $(V_N - V)/V$.

Costin *et al* (2022) derived an asymptotic expression for the upper bound, E_N , on the absolute value of the series approximation error, e_N , as a function of N and the radial coordinate, r. The asymptotic formula for the error bound is

$$E_N \simeq BN^{-b} \left(R/r \right)^N, \tag{13}$$

where R is the radius of the Brillouin sphere, the positive constant b is proportional to the *regularity* (differentiability) of the planet's topography, and the positive constant B is fixed for any given radial line, but, in general, will vary with θ and λ . We call b and B the formula's decay constant and scale factor, respectively. The symbol \simeq , sometimes referred to as 'asymptotically equal to,' means that $E_N/(BN^{-b}(R/r)^N) \to 1$ as $N \to \infty$. The right-hand side of equation (13) serves as a very good approximation to the true error bound only for 'large enough' values of N. In the interests of brevity, we sometimes refer to equation (13) as Costin's formula.

For the rest of this paper, we will use R (rather than R_B) to represent the radius of the Brillouin sphere.

Note that the right-hand side of equation (13) consists of the constant B, the expression N^{-b} which decays as N increases, and the expression $(R/r)^N$, which either grows or decays as N increases depending on whether r is smaller or greater than R, respectively.

In the sections that follow, we will validate equation (13), and explore its implications, using synthetic, constant-density planets for which we can compute the correct values of the potential, V, and gravitational acceleration, g, everywhere in free space above the planet's surface, to hundreds of significant digits (using Mathematica's arbitrary precision arithmetic), and compute the series approximation error, e_N , with a similarly high precision. Comparing E_N to e_N for $N = 1, 2, ..., N_{\text{max}}$ requires us to evaluate the positive constants b and b, for each radial line of interest, so that we can evaluate E_N as a function of N.

Our strategy for estimating b and B is to do so on the Brillouin sphere, where R/r=1. In this setting, e_N should be bound above (for large enough N) by $E_N=BN^{-b}$, and the scaled errors $e_N^*=N^be_N$ should be bound above by $E_N^*=N^bE_N=B$. This suggests an obvious search algorithm for finding b, and once the value for b has been determined, then b is simply the observed upper bound on e_N^* . This strategy is most easily grasped using a concrete example—see section 6.

5.2. The connection of the exponent b (and error decay rate) to smoothness of the topography

The asymptotic decay rate of the sequence of truncation errors $\{e_N\}$ is closely related to the decay rate of the sequence of coefficients $\{a_N\}$ appearing in (12). Call a power series *sufficiently alternating* if the ratio of the number of positive coefficients to the number of negative coefficients through degree N tends to 1 as $N \to \infty$. In practice, the power series V_{∞}^A in equation (12) is almost always of this type. The following is not hard to verify.

Theorem 1. If equation (12) is sufficiently alternating, then the asymptotic bounds for $\{e_N\}$ and $\{|a_N|\}$ differ by a constant (i.e. their ratio is a constant).

Said another way: when the series for the radial restriction of V is sufficiently alternating, then on the Brillouin sphere $S_{\rm Br}$ both $\{e_N\}$ and $\{a_N\}$ asymptotically behave as $\{N^{-b}\}$ for some b>0.

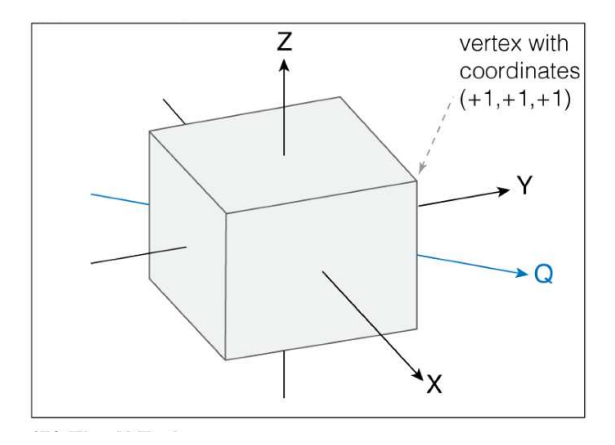
Assuming the planet has a single largest peak (generically this happens almost always), the precise result of Costin *et al* (2022) is that the regularity (smoothness) of the topography in a topographical neighborhood of the peak of the tallest mountain determines the magnitude of b; a smoother neighborhood results in a larger b, and hence a more rapid rate of decrease for the sequence $\{a_N\}$, and hence also $\{e_N\}$ by the above theorem.

Define the function V_S to be the restriction of the potential V to the sphere S. Let the Brillouin sphere be represented by $S_{\rm Br}$. The smoothness of the function $V_{S_{\rm Br}}$ is determined by the smoothness of $V_{S_{\rm Br}}$ in a neighborhood of the point on $S_{\rm Br}$ where that mountain touches $S_{\rm Br}$, which in turn strongly correlates with the smoothness of the topographical neighborhood above, viewed as an open surface in \mathbb{R}^3 . Finally, the smoothness of $V_{S_{\rm Br}}$ directly correlates with the decay rate of the coefficients appearing in the SH series expansion of V_S , in much the same way as the decay rate of the coefficients of the Fourier transform of a 2π -periodic function of one variable f is determined by the smoothness (degree of differentiability) of f on the interval $(-\pi,\pi)$. Similar correlations hold when the planet has finitely many maximal peaks all of the same distance from the origin (as is the case with our cubic planet, discussed next).

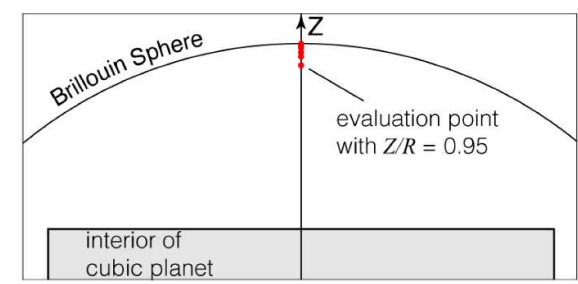
6. The case of a cubic planetoid

6.1. Methodology

We begin with a highly idealized, constant-density 'planet' in the form of a cube (figure 3). This cube has volume $2 \times 2 \times 2 = 8$ and its Brillouin sphere has radius $R = \sqrt{3}$, which is the distance from the center of the cube to each of the eight vertices. We adopt the normalization scheme that $G\rho = GM/8 = 1$, where ρ is the density of the cube. We can compute the gravitational potential, V, and the gravitational acceleration, g, anywhere in free space exterior to the cube, by integrating the standard expressions for V or g at some exterior point P due to an infinitesimal element of volume dv (with mass $dm = \rho dv$) over the cube as a whole. Typically, this classical approach



(A) The X, Y and Z axes pass through the centers of the faces of the cubic planet. The Brillouin sphere has radius $R=\sqrt{3}$, and it touches the planet at just eight points, i.e. the vertices of the cube.



(B) The evaluation points on the Z-axis that are used in this study. Note that the cube does not touch its Brillouin sphere in the X, Z-plane, though it does so, for example, in the Q, Z-plane.

Figure 3. (A) The cubic planet, and (B) The *X*, *Y*-plane (right).

requires numerical integration. But this resort is not necessary for the cube. If the point P lies on one of the three axes, say the positive Z-axis, then, given the resulting symmetry of the problem, it becomes practical to find exact closed-form analytical expressions for V and g as functions of Z, the only non-zero coordinate of P. We did this using Mathematica. The analytical expressions for V or g can be evaluated to hundreds of significant digits using Mathematica's arbitrary precision arithmetic. This provides us with the 'correct' answer, to any desired degree of accuracy, at any chosen evaluation point (figure 3(B)), and facilitates computation of the prediction error associated with a truncated TS approximation for V or g. Analogous results can be obtained for other Platonic solids, in particular for the tetrahedron, which can be viewed as a fundamental building block.

In order to compute the prediction error associated with a TS approximation truncated at degree N, it is necessary to compute the coefficients of this Taylor polynomial. If we set z = R/r = R/Z, then we could, in principle, compute the coefficients in the polynomial approximations for V by successively differentiating the analytical expression for V with respect to z, as seen in the expansion equation (9). In practice this would be prohibitively expensive (computationally), so we compute the series approximation using Mathematica's built-in Series function instead. This approach is viable when our evaluation points are restricted to the positive Z-axis but not for the case of an arbitrarily oriented radial line.

The other advantage to restricting our evaluation points to the positive Z-axis is that along this radial line the magnitude of gravitational acceleration $g = \|\mathbf{g}\| = \|\nabla V\| = |\partial V/\partial r| = |\partial V/\partial Z|$. Typically, algebraic expressions for $\|\nabla V\|$ can be derived in closed form, but they are much more involved than the expression for V and so in general do not allow for the algebraic computation of Taylor polynomial approximations. However, the expression for $|\partial V/\partial Z|$ is much simpler (it can be stated in four pages), making the computations more manageable.

Having computed the exact solution for V and its TS approximation complete through degree N (for $N = 1, 2, ..., N_{\text{max}}$), we can now compute the series approximation error, e_N , and implement the strategy outlined in section 5 for finding the constants b and b in the asymptotic formula for the upper bound on the absolute value of series approximation error

6.2. Searching for constants b and B, and validating the results

As noted in section 5, if we choose the correct value for b the scaled errors $e_N^* = N^b e_N$ should be bounded above by $E_N^* = N^b E_N = B$, which is a constant. We illustrate this strategy in figure 4.

If we guess that b=3.3 we see that the local upper and lower bounds on e_N^* converge as N increases (figure 4(A)). In contrast, if we guess that b=3.7 we see that the local upper and lower bounds on e_N^* diverge as N increases (figure 4(C)). But when we set b=7/2=3.5, as soon as N exceeds about 150, the upper and lower bounds (B and -B) are fixed or horizontal, and, to a good approximation, B=25.94. Clearly, asymptotic behavior was achieved quite quickly. The other interesting aspect of this sub-plot is that once asymptotic behavior is fairly well established, the scaled prediction error for the series approximation for V is seen to oscillate between the upper and lower bounds. We shall discuss the nature of oscillatory errors in some detail in section 7.3.

Having found the values of b and B in the asymptotic expression, equation (13), for the radial line corresponding to the positive Z-axis, we can now validate this formula for values of R/r other than 1. We do this at a number of evaluation points on the Z-axis, at varying depths below the Brillouin sphere (the red dots in figure 3(B)). The errors e_N were computed for $N = 1, 2, ..., N_{\text{max}}$, where $N_{\text{max}} = 3500$, at each of the evaluation points. Because e_N varies by many orders of magnitude over this range of N-values, it is not practical to use a linear

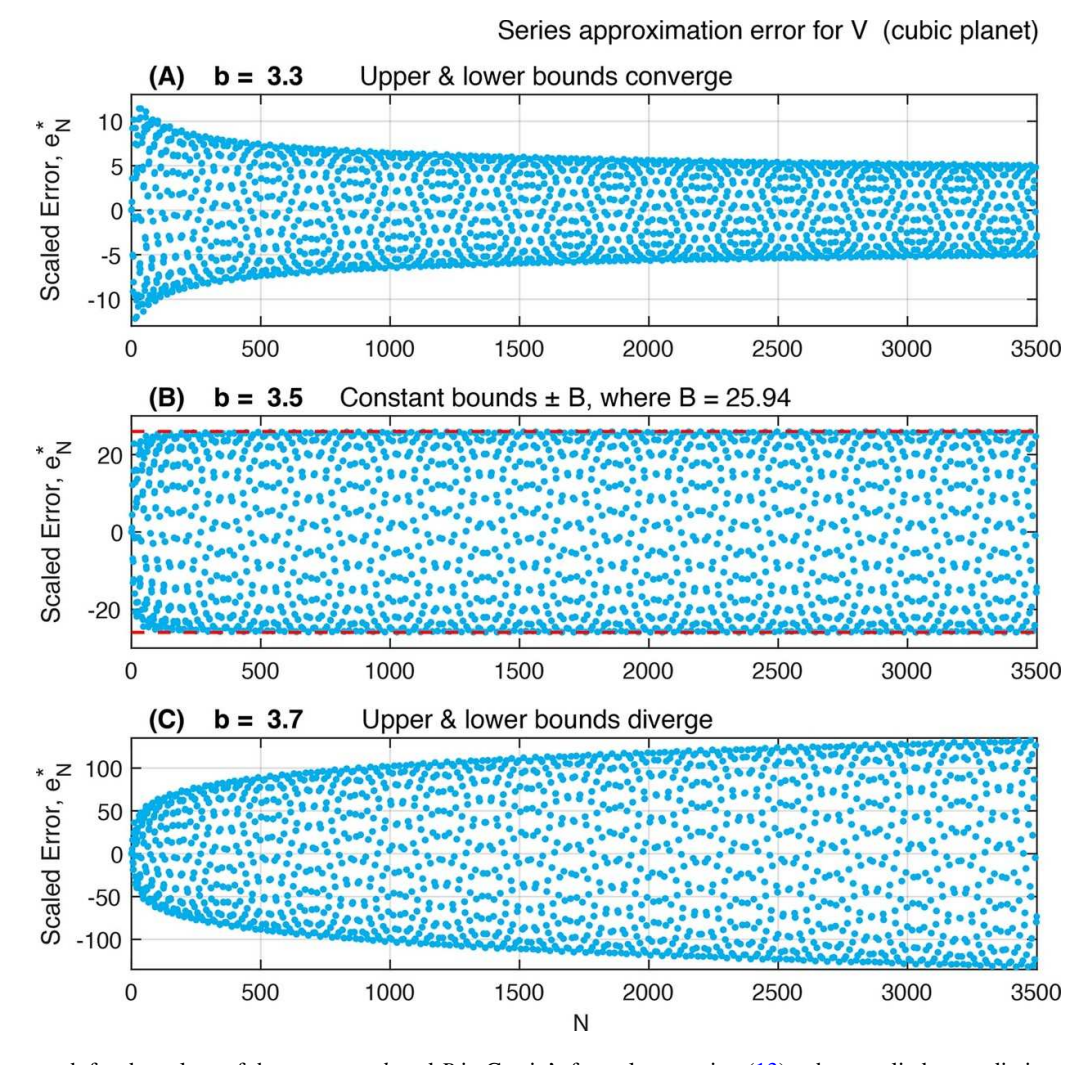


Figure 4. The search for the values of the constants b and B in Costin's formula, equation (13), when applied to prediction error in the series approximation for V (on the positive Z-axis above the cubic planet). The search for b is realized where the positive Z-axis intersects the Brillouin sphere, where R/r = R/Z = 1. The dashed red line in the central plot shows the constant upper and lower bounds, once asymptotic behavior is established.

scale for the vertical axis used in plots of e_N versus N. It is necessary to use a logarithmic scale instead, and this requires us to plot the logarithm of the *absolute value* of e_N versus N (these are the blue dots in figure 5). The e_N are oscillating between upper and lower bounds, as seen previously with the scaled errors e_N^* in figure 4, but now the negative values of e_N are represented using their (positive) absolute values in the new plots. The sparse sub-set of blue dots near the bottom of each cloud of blue dots represent those values of e_N that are unusually close to zero. Such values manifest the oscillations (and therefore zero-crossings) in the e_N spectrum.

The predictions of the asymptotic formula for the upper bound E_N are also shown using red dashed lines in each of the three sub-plots of figures 5(A)–(C), which correspond to evaluation points with Z/R = 0.999, 0.996, and 0.990, respectively. Obviously, these asymptotic curves are shown using the same logarithmic scaling. The agreement between the upper limits of the directly computed $|e_N|$ and the theoretical curve E_N is all the more pleasing given that we developed the

asymptotic expression for E_N many months before we found a way to compute the series prediction errors on the positive Z-axis above the cube with the necessary degree of accuracy.

6.3. The behavior of series approximation error for V beneath the Brillouin sphere

Having validated the asymptotic formula for the upper bound E_N , we can plot these bounding curves for eight different evaluation points on a single semi-log plot, to illuminate the phenomenology of divergence-driven series prediction error. But rather than work with the error $V_N - V$ we will plot the upper bounds for the magnitude of relative error $(V_N - V)/V$, instead (figure 6). These curves are labeled in terms of the value of r/R = Z/R of the corresponding evaluation points, which lie in the range 0.950–0.999.

We define $N = N_{\text{opt}}$ to be the value of the series truncation degree N where the magnitudes of both the error, e_N ,

Series error for V: directly computed versus upper bound from asymptotics 0 -2 upper bound, E_N -4 -6 -8 -10 0 500 1000 1500 2000 2500 3000 3500 (B) Z/R = 0.9960 directly computed e N -2 upper bound, E_N -4 -6 -8 -10 0 500 1500 1000 2000 2500 3000 3500 (C) Z/R = 0.9904 directly computed e 2 upper bound, E, 0 -2 -4 -6 0 500 1000 1500 2000 2500 3000 3500 N

Figure 5. Directly computed prediction errors e_N for series approximations for V, complete through degree N (blue dots), compared with the asymptotic expression for the upper bound E_N on these errors, for three evaluation points on the positive Z-axis. The evaluation points lie between the cubic planet and its Brillouin sphere. The evaluation points for plots (A)–(C) have R/r = R/Z = 0.999, 0.996 and 0.990, respectively. Note the use of the base-10 logarithm: the error bound curve in (C) has values that range over 10 orders of magnitude or decades.

and relative error, e_N/V , reach their minimum or *optimal* values (for given r/R = Z/R). These turning points are marked with the blue circles in figure 6. We shall show that $N = N_{\text{opt}}$ depends on b but not on B. We can understand this behavior by examining the components of the error bound formula, equation (13), that is $E_N = BN^{-b}(R/r)^N$, where r = Z. We see that below the Brillouin sphere:

- For $N < N_{\text{opt}}$, N^{-b} dominates $(R/Z)^N$, and the error declines
- For $N > N_{\text{opt}}$, $(R/Z)^N$ dominates N^{-b} , and the error increases as N increases.

Since exponential growth manifests as a straight line on this semi-log plot, figure 6 suggests that for $N \gg N_{\text{opt}}$, error

increases exponentially with increasing N. This is easily understood. When $N \gg N_{\rm opt}$, the rate of change of E_N is dominated by the rate of change of $(R/Z)^N$, and this term grows exponentially with N.

This discussion of the relative impacts of N^{-b} and $(R/Z)^N$ focuses on the *mathematical* behavior of Costin's formula, equation (13). But is it possible to make a physically more intuitive interpretation of this behavior? We offer the following thoughts. Increasing N reduces series approximation error by providing the truncated series with greater degrees of freedom, allowing V_N to better 'follow' the variations in the true potential V on the radial line in free space (where $(R/Z)^N$ is bounded as a function of N). Increasing N allows V_N to better resolve the fine details in the structure of V(r). We can also take the view that this improvement in the performance

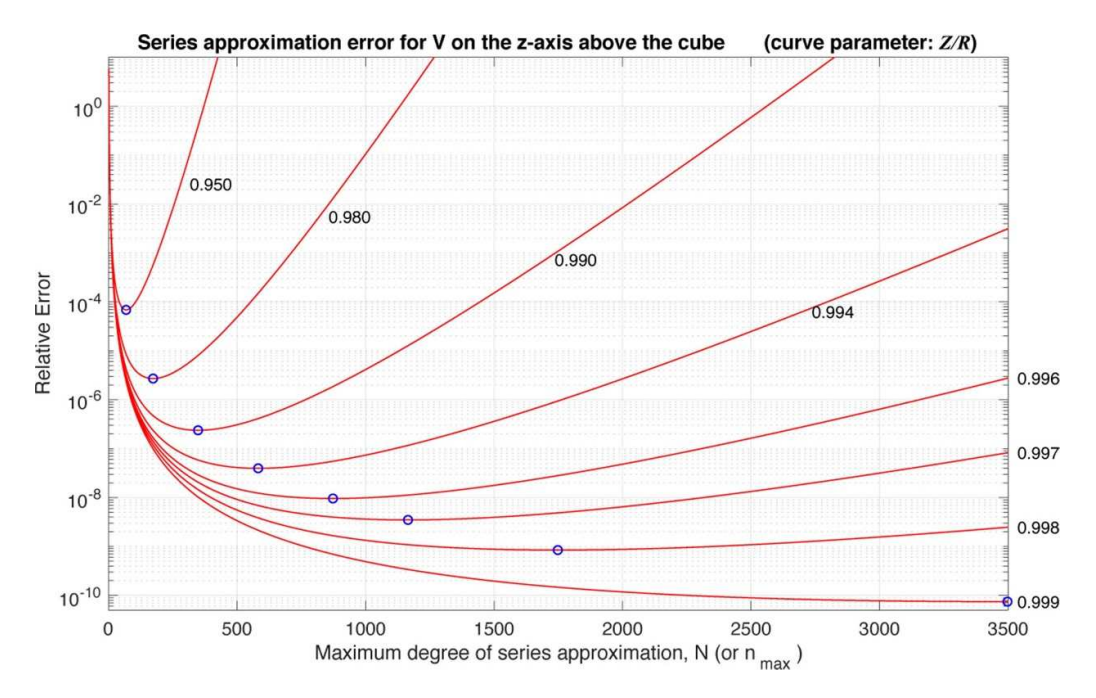


Figure 6. The upper bound on the relative prediction error versus the truncation degree N of the series approximation for V. The eight curves show the relative error spectra for eight evaluation points on the positive Z-axis with values of r/R = Z/R ranging between 0.95 and 0.999. Each curve is labeled with the corresponding value of Z/R. The blue circles indicated the location of the minimum relative error on each curve. This turning point occurs when $N = N_{\text{opt}}$. Clearly, $N = N_{\text{opt}}$ declines as the evaluation point lies deeper and deeper beneath the Brillouin sphere, where Z = R.

of the polynomial approximation is achieved by reducing its 'error of omission' or 'truncation error' (i.e. the impact of omitting from the Taylor polynomial all terms in the infinite TS with degree greater than N). In contrast, and simultaneously, increasing N also causes an increase in the series prediction error beneath the Brillouin sphere because, as it lengthens, the Taylor polynomial increasingly manifests the divergence of the infinite TS. These 'enhancing' and 'degrading' tendencies co-exist and compete. Improving resolution is more important than suppressing divergence when $N < N_{\rm opt}$, because the speed of improvement (as $N \rightarrow N+1$) is greater than the speed of degradation. The reverse is true when $N > N_{\rm opt}$. Thus, $N_{\rm opt}$ serves as the cross-over point in the competition between increasing the degrees of freedom available to the Taylor polynomial and reducing its divergence.

So far we have emphasized how series approximation error changes with N when depth beneath the Brillouin sphere is held constant. It is also useful to track e_N and E_N when we fix N and vary Z instead. We did this by setting N = 3500, and directly computing relative error e_N/V and evaluating the relative error bound E_N/V at 30 different values of Z. The results are shown in figure 7. At first it might seem strange that there is a significant gap or offset between the directly computed errors and the error bound predicted using the asymptotic formula. But recall that the actual errors e_N are oscillating between E_N and $-E_N$ (figure 5), and therefore there are many N-values for which $|e_N|$ will be smaller than E_N . There is only one value of N in figure 7. The presence of the 'gap' is not surprising; though it is interesting that the size of this gap does not change significantly over this range of depth values. The explanation for this will become apparent in section 6.6.

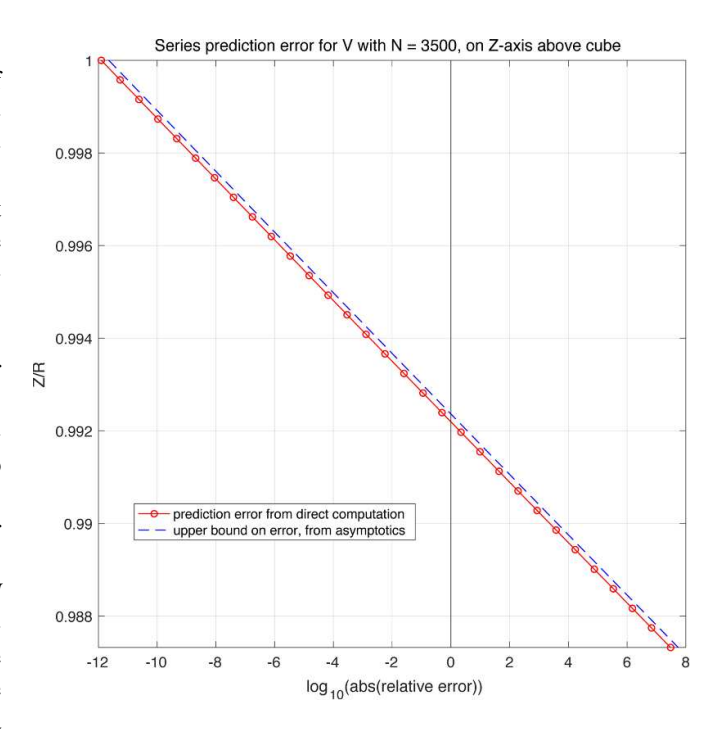


Figure 7. The absolute value of relative prediction error for V evaluated on the Z-axis beneath the Brillouin sphere, when N=3500. The directly computed error is shown using red circles and the upper bound implied by Costin's formula using a blue dashed line.

The most obvious feature of figure 7 is that the observed error profile (e_N versus Z/R) and the corresponding E_N -curve both appear to be very nearly straight lines on this semi-log

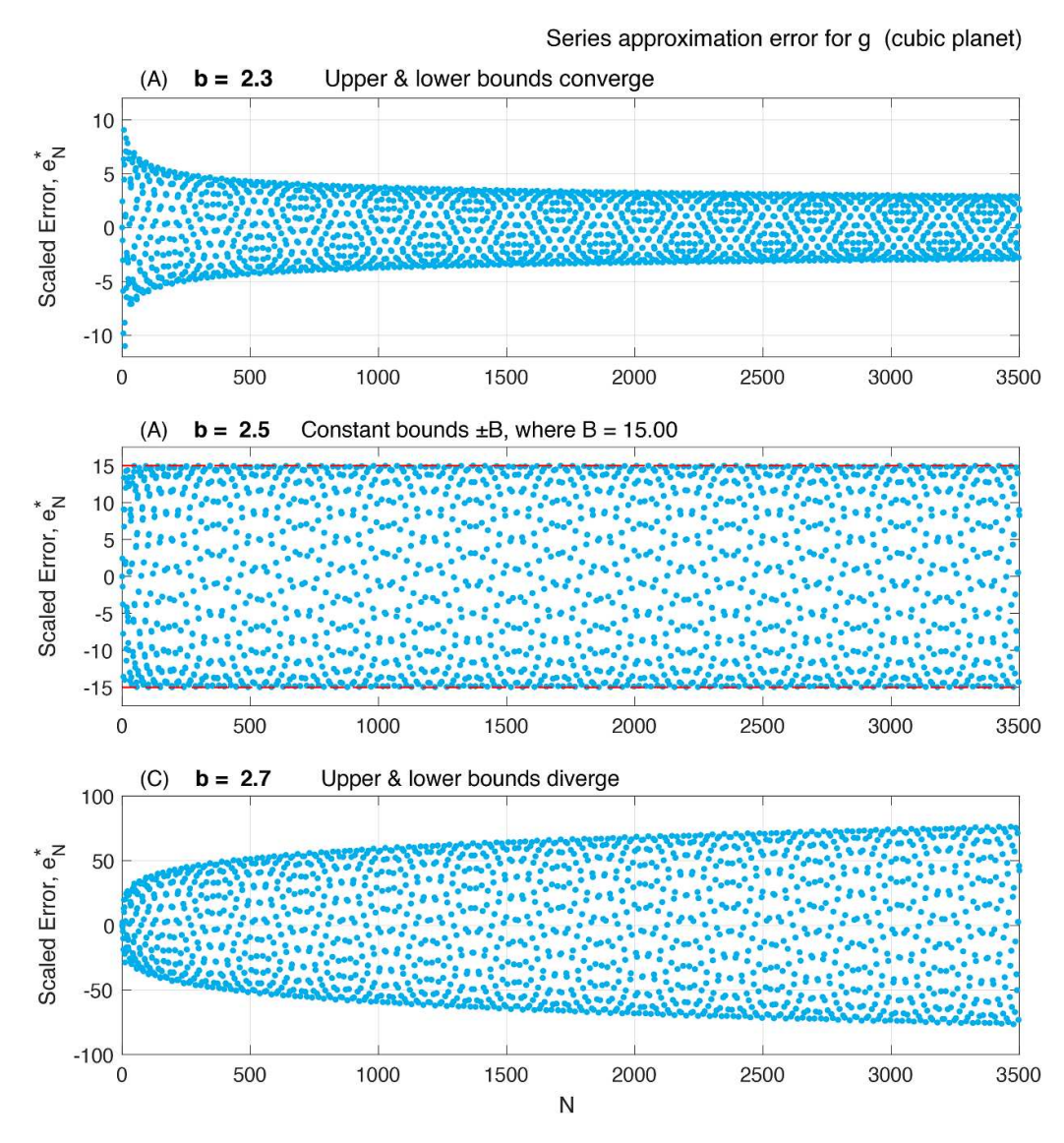


Figure 8. The search for the values of the constants b and B in the asymptotic formula, equation (13), when applied to prediction error in the series approximation for g on the positive Z-axis above the cubic planet. The search for b is realized where the positive Z-axis intersects the Brillouin sphere, where R/r = R/Z = 1. The dashed red line in the central plot shows the constant upper and lower bounds, once asymptotic behavior is established.

plot. This implies that series prediction error is increasing exponentially with depth below the Brillouin sphere. Suppose we define depth d = R - r = R - Z, then it is easy to show that if $d_{\text{max}} \ll R$ (for example $d_{\text{max}}/R < 0.01$) then Costin's formula implies that, to a very good approximation, E_N should increase exponentially with d in the depth range $0 < d < d_{\text{max}}$. Specifically, for all $d \ll R$, the asymptotic approximation for the upper bound on series error can be approximated thus

$$\log E_N = \log E_N^{Br} + Nd/R, \tag{14}$$

where log refers to the natural logarithm, and $E_N^{Br} = BN^{-b}$ is the value of the error bound E_N at the intersection of the positive Z-axis and the Brillouin sphere (where R/r = R/Z = 1). Given that b and B are constants, if N is held fixed, then the first term on the right-hand side of equation (14) is a constant, and d is the only variable in the second term.

6.4. Gravitational acceleration on the Z-axis beneath the Brillouin sphere

As we noted in section 6.1, we can estimate the gravitational acceleration g anywhere on the positive Z-axis beneath the Brillouin sphere and compare it to the TS approximation for g, which we obtain by forming the Z-derivative of the TS approximation for V. This allows us to compute e_N for g, and thus search for the constants for b and b in Costin's formula when it is applied to g rather than V. The analysis of Costin et a (2022) implies that since $g = \partial V/\partial Z$ we should expect that $b^g = b^V - 1 = 7/2 - 1 = 5/2$. This is confirmed when we perform a search for b^g , much as we previously searched for b^V in figure 4. We see that when we plot the scaled errors E_N^* versus N for g, the error bounds converge if we assume that b = 2.3 (figure a (A)) and diverge if we assume that a (figure a (C)). But when we set a =

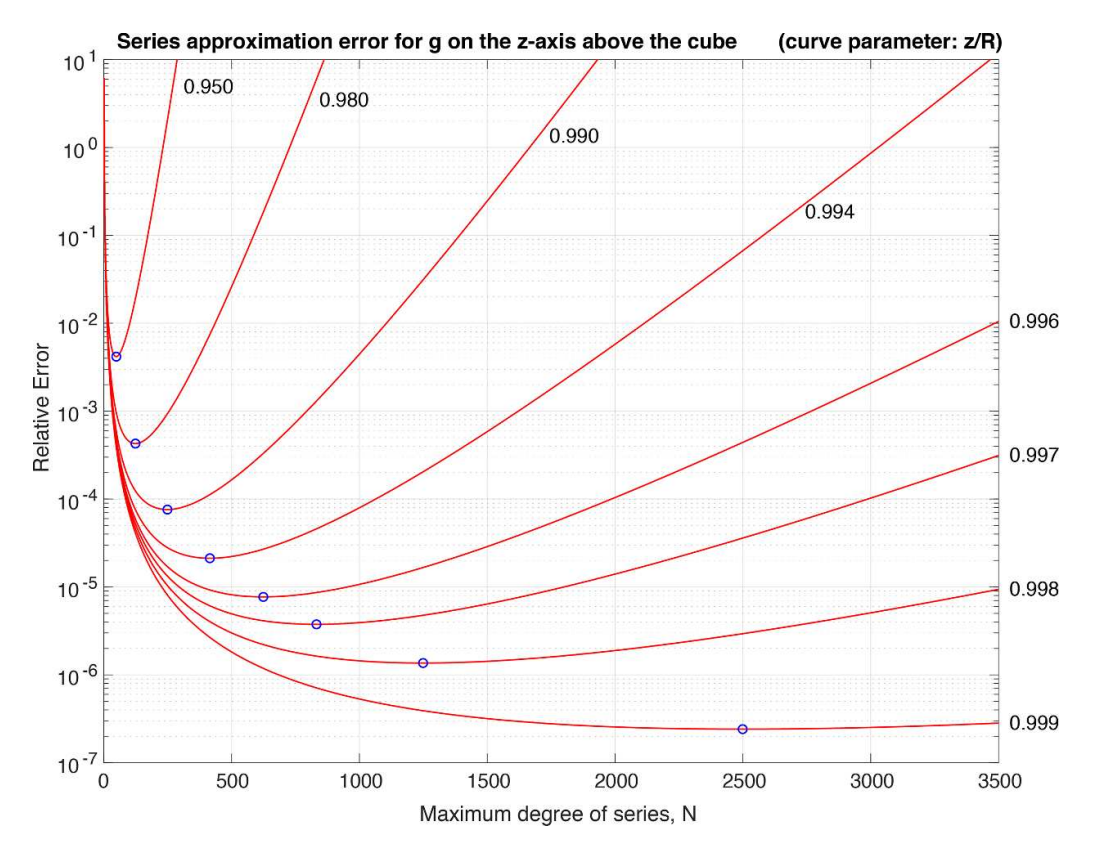


Figure 9. The upper bound on the relative prediction error versus the truncation degree N of the series approximation for g. The eight curves show the relative error spectra for eight evaluation points on the positive Z-axis with r/R = Z/R values ranging between 0.95 and 0.999. Each curve is labeled with the corresponding value of Z/R. The blue circles indicated the location of the minimum relative error on each curve. This turning point occurs when $N = N_{\text{opt}}$. Clearly, $N = N_{\text{opt}}$ declines as the evaluation point lies deeper and deeper beneath the Brillouin sphere, where Z = R. Compare these curves with those in figure 6.

become 'fixed' or horizontal. We see that for g, B = 15.00. This allows us to find the g equivalent to figure 6, that is, the relative error spectra for g shown in figure 9.

Note that the onset of divergence and increased prediction error occurs 'sooner' for g than for V, in terms of its development as a function of N, and as a function of depth as we descend beneath the Brillouin sphere (figure 9 versus figure 6). This is a natural consequence of the differentiation of the potential.

6.5. On the optimal value of N

We need to know both b and B in Costin's formula in order to evaluate the upper bound of divergence-driven prediction error. But to compute N_{opt} , we need only knowledge of b. To find the optimal value of N we replace N in equation (13) with a continuous real variable u. We take the derivative of E_N with respect to u, set that derivative to zero, and solve for the particular value of u at the turning point, yielding

$$u_{\rm TP} = b/\log(R/r). \tag{15}$$

As u_{TP} is generally not an integer, we set N_{opt} to be the largest integer less than or equal to u_{TP} .

To compute the vertical profile of $N_{\rm opt}$ for V and g, we must set b=7/2 or b=5/2, respectively. We have done

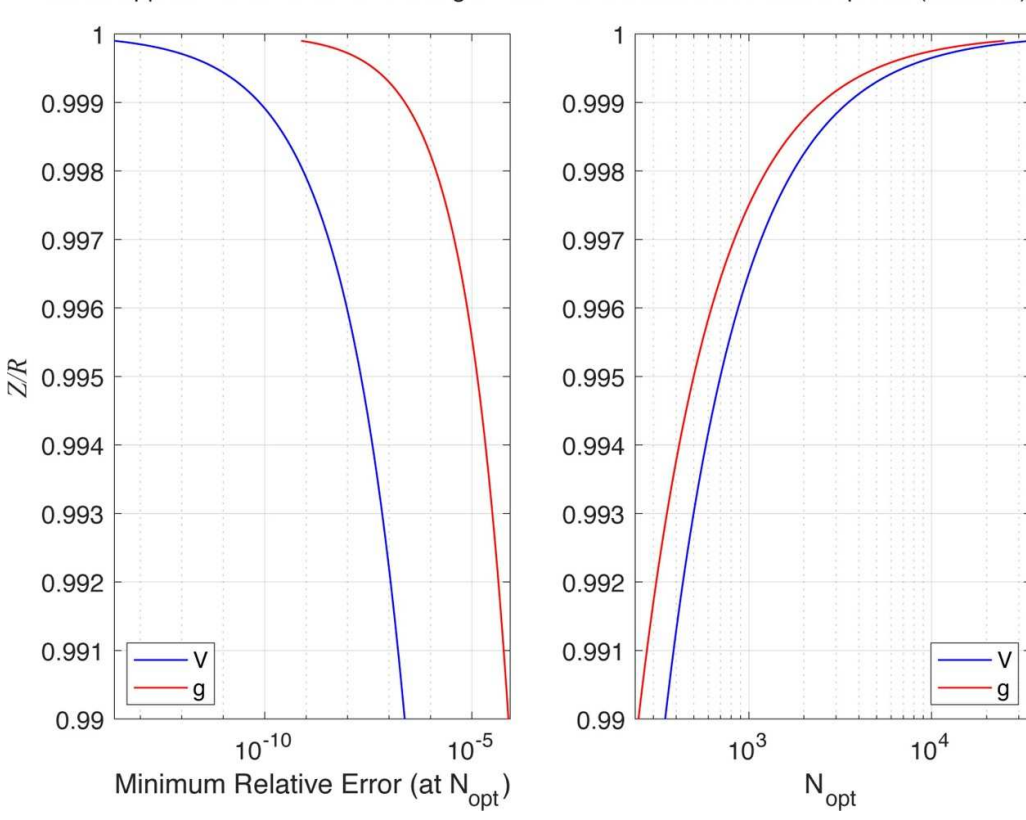
this in figure 10(B). Having computed $N_{\rm opt}$, it is a simple matter to compute the upper bounds on relative error E_N/V and E_N/g for V and g, respectively, when $N=N_{\rm opt}$. This provides an upper bound on the minimum value of relative error at each value of R/r=R/Z. We plot these minimum relative error profiles in figure 10(A). As we saw previously, divergence drives much larger relative approximation errors for g than for V, and the onset of divergence occurs (at any given depth below the Brillouin sphere) at smaller values of N.

6.6. Asymptotic bounds on the Taylor series coefficients

In section 5.2, we claimed that the asymptotic behavior of approximation error e_N is closely related to the asymptotic behavior of the coefficients of the TS along the same radial line. In this section, we will show that in the asymptotic limit, the coefficients $\{a_n\}$ in equation (12) have an upper bound A_n given by

$$A_n \simeq K n^{-k},\tag{16}$$

where k and K are positive constants. When the TS coefficients for a given radial line are oscillating around zero (which is the case for nearly all radial lines) then their lower bound is $-A_n$. It is sometimes convenient to plot the coefficients using



Series approximation error for V and g on the Z-axis below the Brillouin sphere (radius R)

Figure 10. (A—left) The upper bound on the minimum relative error as a function of Z/R, which is the value of the relative error when $N = N_{\text{opt}}$. This is shown for the series approximation error for V and g. (B—right) The vertical profile of N_{opt} for V and g, again for a range of Z/R values on the positive Z-axis above the cube.

a logarithmic scale, requiring us to plot $|a_n|$ rather than a_n . In this case, the upper bound remains the same and there is no lower bound.

The asymptotic formula, equation (16), implies that the scaled coefficients $a_n^* = n^k a_n$ should be bound above by $A_n^* = n^k A_n = K$. (The same is true if we define $a_n^* = n^k |a_n|$, so we can use a semilog plot). In the case of the series approximation for V, this expectation is true if we select k = 7/2 (figure 11). This allows us to determine that K = 42.31. While the asymptotic constant k for V is identical to the asymptotic constant k for V, this equality does not extend to the associated constants E and E.

We perform a similar analysis for the coefficients of the Taylor polynomial approximation for g and find that k = 5/2 and K = 24.45 (figure 12). Once again see that k for g matches the value of b for g, but this equality does not extend to K and B.

However, there are suggestions of proportionality since we find that $K^V/B^V \approx K^g/B^g \approx 1.63$. Similarly, we find that $K^V/K^g \approx B^V/B^g \approx 1.73$. The radius of the Brillouin sphere for the cube is $R = \sqrt{3} \approx 1.73$. So perhaps the underlying asymptotic relationship is $K^V/K^g = B^V/B^g = R$. We are better able to assess these intriguing relationships in the next section, when we work with a synthetic polygonal planet and examine the phenomenology of divergence and asymptotic behavior on many different radial lines.

7. Investigating Taylor series divergence in free space exterior to a polyhedral planet

There are obvious problems and limitations with our use of a 'cubic planet.' First, it is nothing like the shape of the Earth or Moon, or any other terrestrial planet. We have performed similar studies of other regular Platonic solids, but they are not Earth-like either, particularly in terms of our ability to simulate fairly realistic topography. Secondly, in terms of our analytical methodology, we were limited to working on the positive Zaxis which passed through the center of one of the faces of the cube. We could do the same on the negative Z-axis, or the positive and negative X and Y axes, but given the symmetry of this cubic planet, this would not introduce any new insights. We need a new approach that allows us to examine divergence in free space beneath the Brillouin sphere along any radial line, and which allows us to simulate planets that are more realistic in terms of their morphology. This new approach has to allow us to compute V and the components of the gravitational acceleration vector g anywhere in free space external to the planet with arbitrary levels of numerical precision, allowing us to compute prediction error $V - V_N$, or relative prediction error $(V - V_N)/V$, to hundreds of significant digits, so we can track the evolution of divergence with changing N or changing depth beneath the Brillouin sphere, even when the intensity or impact of divergence is still very small.

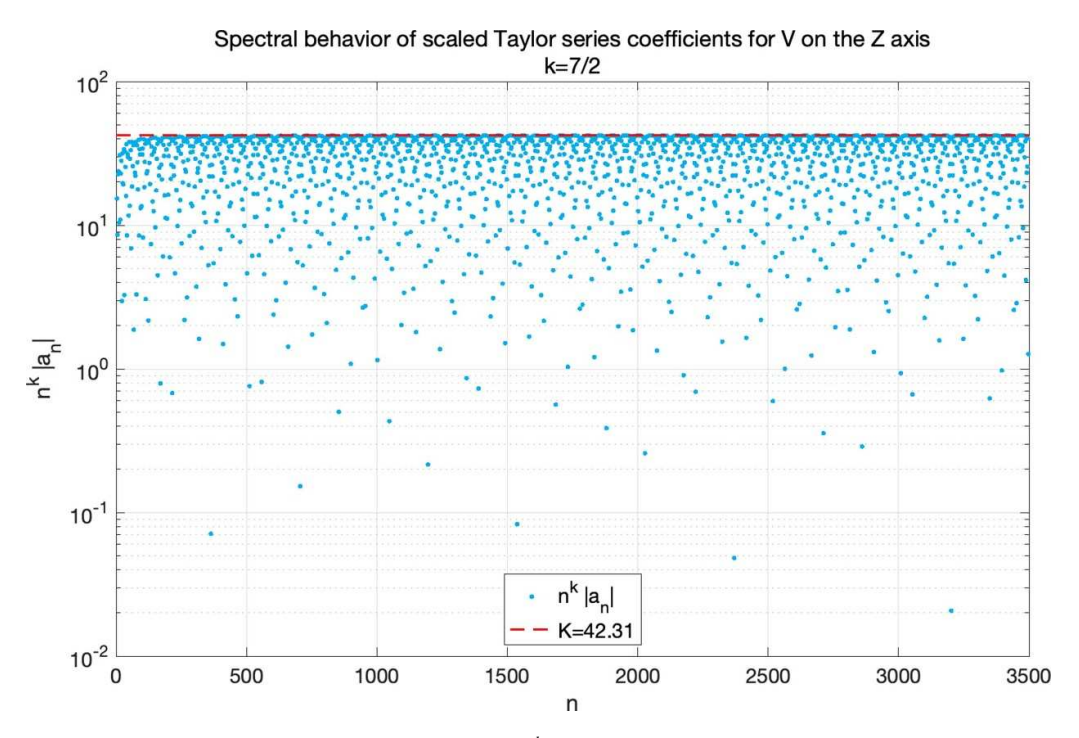


Figure 11. Asymptotic behavior of the scaled absolute values, $a_n^* = n^k |a_n|$, of the Taylor polynomial coefficients for V restricted to the positive Z-axis. A constant upper bound is found only if k = 7/2. Once asymptotic behavior is fully established, when N is greater than about 200, the upper bound on a_n^* is the constant K = 42.31. The scaled coefficients $n^{-k}a_n$ are oscillating between -K and K, but the blue dots represent the scaled absolute values of the coefficients, $n^k |a_n|$, which are always positive. The sparse set of dots seen near the bottom of the plot represent near-approaches to zero as the oscillating coefficients change sign.

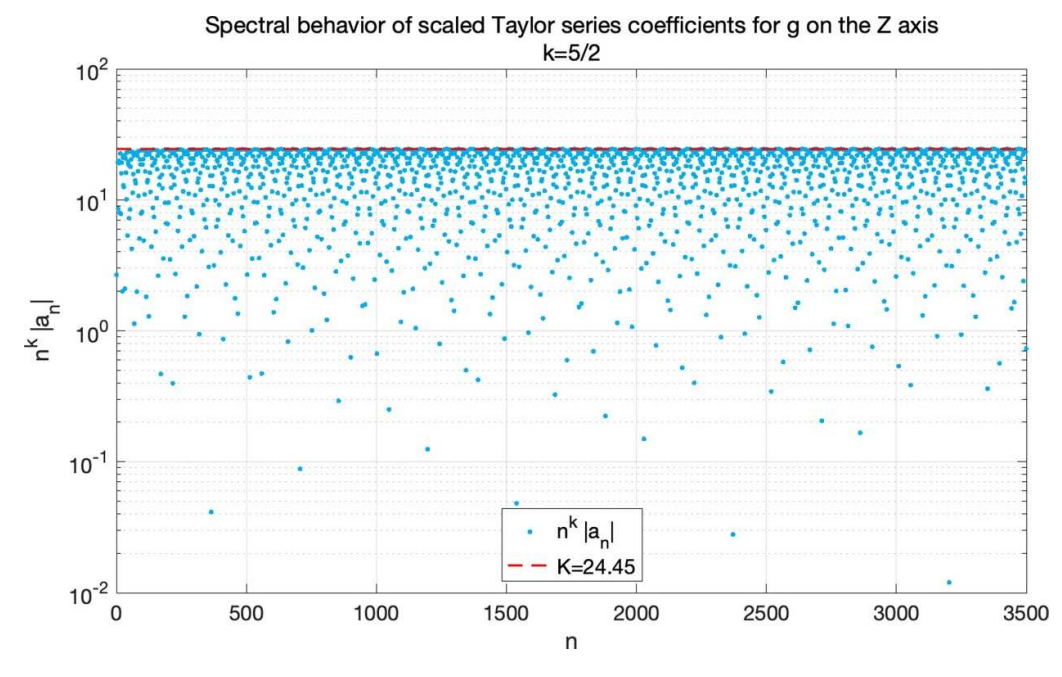


Figure 12. Asymptotic behavior of the scaled absolute values, a_n^* , of the Taylor polynomial coefficients for g restricted to the positive Z-axis. A constant upper bound is found only if k = 5/2. Once asymptotic behavior is fully established, when N is greater than about 100, the upper bound on a_n^* is the constant K = 24.45.

For these reasons we decided to adopt the flexible simulation framework of a constant-density polyhedral planet based on the approach of Werner (1994).

7.1. A polyhedral, constant-density planet

Werner (1994) provided a means to compute the gravitational field exterior to a homogeneous (constant density) planet whose surface is a polyhedron composed of an arbitrary number of triangular faces. He did so by providing closed-form expressions for exterior gravitational potential V and for exterior gravitational acceleration \mathbf{g} . These algebraic solutions were derived using Gauss' divergence theorem and Green's theorem, one triangular face at a time, and summed over the entire polyhedron. They are *exact* solutions.

We employ Werner's algebraic expressions for V, but we choose to compute $\mathbf{g} = \nabla V$ by taking numerical derivatives of V, using arbitrary precision arithmetic. As with the cube, we developed our codes for the polyhedral planet using Mathematica. We can use this code to compute the 'correct answer' for V and \mathbf{g} to hundreds or thousands of significant digits, and—as we did for the cubic planet—to compute a series approximation for V restricted to any radial line, to similar levels of numerical precision. We often compute the series approximation for the radial component g_r of \mathbf{g} by forming the numerical derivative (with respect to r) of V. Recall that in Cartesian coordinates

$$\mathbf{g} = \nabla V = \frac{\partial V}{\partial \mathbf{x}} \hat{\mathbf{x}} + \frac{\partial V}{\partial \mathbf{y}} \hat{\mathbf{y}} + \frac{\partial V}{\partial \mathbf{z}} \hat{\mathbf{z}} = g_x \hat{\mathbf{x}} + g_y \hat{\mathbf{y}} + g_z \hat{\mathbf{z}}, \quad (17)$$

and in spherical coordinates

$$\mathbf{g} = \nabla V = \frac{\partial V}{\partial r}\hat{\mathbf{r}} + \frac{1}{r}\frac{\partial V}{\partial \theta}\hat{\boldsymbol{\theta}} + \frac{1}{r\sin\theta}\frac{\partial V}{\partial \lambda}\hat{\boldsymbol{\lambda}} = g_r\hat{\mathbf{r}} + g_\theta\hat{\boldsymbol{\theta}} + g_\lambda\hat{\boldsymbol{\lambda}}.$$
(18)

For any nearly-spherical planet $g_r >> g_\theta$ and $g_r >> g_\lambda$ and therefore $g = \|\mathbf{g}\| \approx g_r$ and $|(g - g_r)/g| << 1$. In most settings, divergence-driven approximation error in g is dominated by the approximation error in g_r . So, we can usually reduce our computational costs by a factor of 3 by computing approximation error in g_r and using it as a proxy for the approximation error in g_r . This can lead to significant reductions in computational expense when the polyhedral planet has a large number of triangular faces. The key idea here is, if the prediction error for g_r is growing very strongly, the same would be true of the prediction error for g_r .

7.2. Building a synthetic polyhedral planet

Constant-density polyhedral planets have a greater utility than one might first imagine, in that a linear combination of such planets can be used to construct layered planets with piecewise constant density. The upper and lower boundaries of all but the innermost of the constant density layers would be convex polygons, and the thickness of each layer could be laterally variable. In this work, we will focus on homogeneous

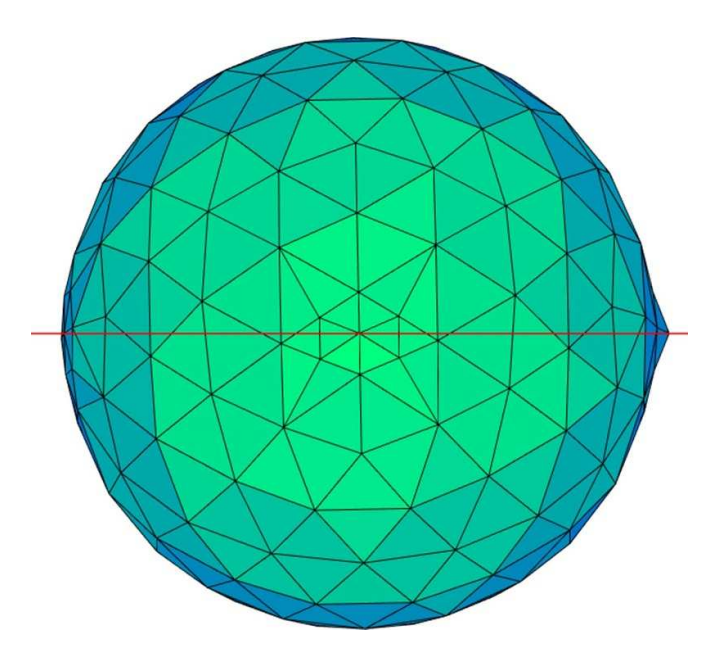


Figure 13. Local densification of the icosphere at the site of the highest mountain, in the center of the plot. Similar densification occurred at the location of the second highest mountain summit, seen at the right limb of the polyhedron. Similar densifications occurred at the antipodes of both mountains. Both mountains have six triangular faces as their flanks.

planets, and defer the modeling of layered planets to a sequel publication.

We begin by constructing a polyhedron in which all the triangular faces have vertices with equal radial coordinates $r = R_s$. Thus the polygon approximates a sphere of radius R_s . In our first study we set $R_s = 1$. To triangulate this sphere, so as to produce a geodesic polyhedron, we use a standard approach, described by Tegmark (1996), in which the triangular faces of an icosahedron are divided into a set of smaller triangles, and all the vertices are projected onto the sphere that circumscribes the icosahedron. The number of triangular faces depends on the number of times each triangle—starting with the 20 triangular faces composing the original icosahedron is divided into four new triangles. The triangular faces of this nearly spherical polyhedron, sometimes referred to as an icosphere, are not equilateral triangles, but they are roughly similar in terms of their edge lengths. We densified the icosahedron twice, resulting in a polyhedron with 162 vertices and 320 faces. Six triangles meet at every vertex, except for the 12 vertices of the original icosahedron, where only five triangular faces meet.

We decided to produce two giant mountains by increasing the radial coordinate r of two (well-separated) vertices to 1.05 and 1.1, respectively. To reduce the width of the base of these mountains we performed a local densification (figure 13) of two triangles whose centroids were located about 95 degrees apart, and did the same for the antipodal triangles. This ensured that the antipode to each 'mountain top,' or summit vertex, was itself a vertex. Once this local densification was completed, the polyhedron had 182 vertices and 360 faces. We

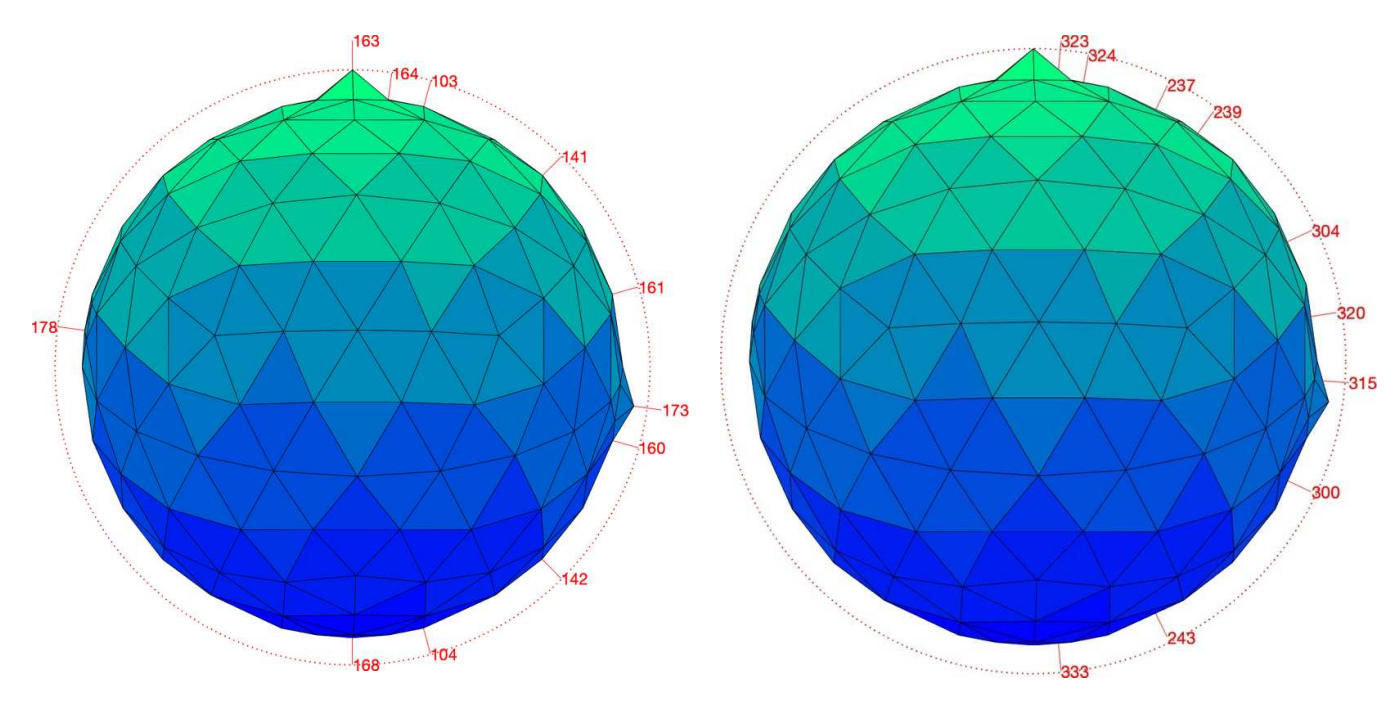


Figure 14. Selected vertices of the 'two-mountain polyhedron' are indicated using their indices. The summit vertex for the tallest mountain (with r=1.1) has index 163, and the summit vertex of the second mountain (with r=1.05) has index 173. The intersection of the Brillouin sphere with the plane that passes through the origin and the two summit vertices is indicated using the dotted red line. Vertex 168 is antipodal to vertex 163, and vertex 178 is antipodal to vertex 173. From this perspective, we can see only two of the six triangular faces that flank the highest mountain.

then adjusted the radial coordinate of a single vertex to make each mountain. Note that the pattern of local densification (subdivision of triangular faces) is such that each mountain takes the form of an hexagonal pyramid (figure 13).

Each vertex and each triangular face has a unique index, and we label some of these elements in figures 14 and 15.

After the summit vertices 163 and 173 were displaced radially outwards, to produce the mountains, our final step was to rotate the coordinate system so that the summit vertex for the highest mountain was located at the 'North Pole' (on the positive *Z*-axis), and the 'Greenwich Meridian' ($\lambda = 0$) passes through the summit vertex of the second, smaller mountain. The summit of the smaller mountain has a latitude of 7.853°S (so $\theta = 97.853^{\circ}$). The singular radial line passes through vertex 163, and the complementary radial line passes through vertex 168.

Of course, the two mountains on our polyhedral planet would be absurdly large if we wished to evoke an Earth-like planet. The reason we designed this synthetic planet in this way was (i) to allow us to assess series divergence above the planet's surface but deep beneath its Brillouin sphere, and (ii) to produce large signals in the rate at which the asymptotic parameters K and B change 'laterally' in response to topography. The larger the mountain, the larger the response. These mountains are so large that the center of mass of the planet has Cartesian coordinates

Figure 15. Selected faces of the 'two-mountain polyhedron' are indicated using their indices. Each face is labeled at its centroid. Thus face 323 constitutes part of the flank of the highest mountain, and face 324 lies on the flat lowlands immediately adjacent to this mountain. Face 315 constitutes part of the flank of the smaller mountain.

(X,Y,Z) = (0.00022636, -0.0000024, 0.0004306), significantly displaced from the center of the original sphere, which remains the origin of our coordinate system. The volume, V, of this mountainous polyhedron is 4.054604. We emphasize that every vertex describing the final polyhedron has r=1 except for the two mountain summit vertices (with r=1.05 and r=1.1).

As with the cubic planet, it is convenient to adopt a normalization scheme. We chose the uniform density, ρ , for the planet such that $G\rho = 2$.

7.3. Bounding series coefficients and prediction error for V

We begin by assessing the behavior of the TS coefficients for V on the radial line passing through the centroid of triangular face 324 (figure 15). As before with the cubic planet, we search for the asymptotic parameters k and K, which were defined in equation (16). We find that k = 7/2 on this radial line (figure 16). As we shall see, we find that k = 7/2 on every radial line except the singular radial line and its complement. This is true whether the radial line passes through a vertex, an edge, or a face of the polyhedron.

We estimated the wavelength, Λ , of the oscillation—after asymptotic behavior seemed well established—by locating the positive peaks and determining the mean distance between them. We found that $\Lambda \approx 35.1$.

After we made a similar analysis for many other radial lines we realized that Λ was inversely proportional to the angle, α , between the radial line under consideration and the

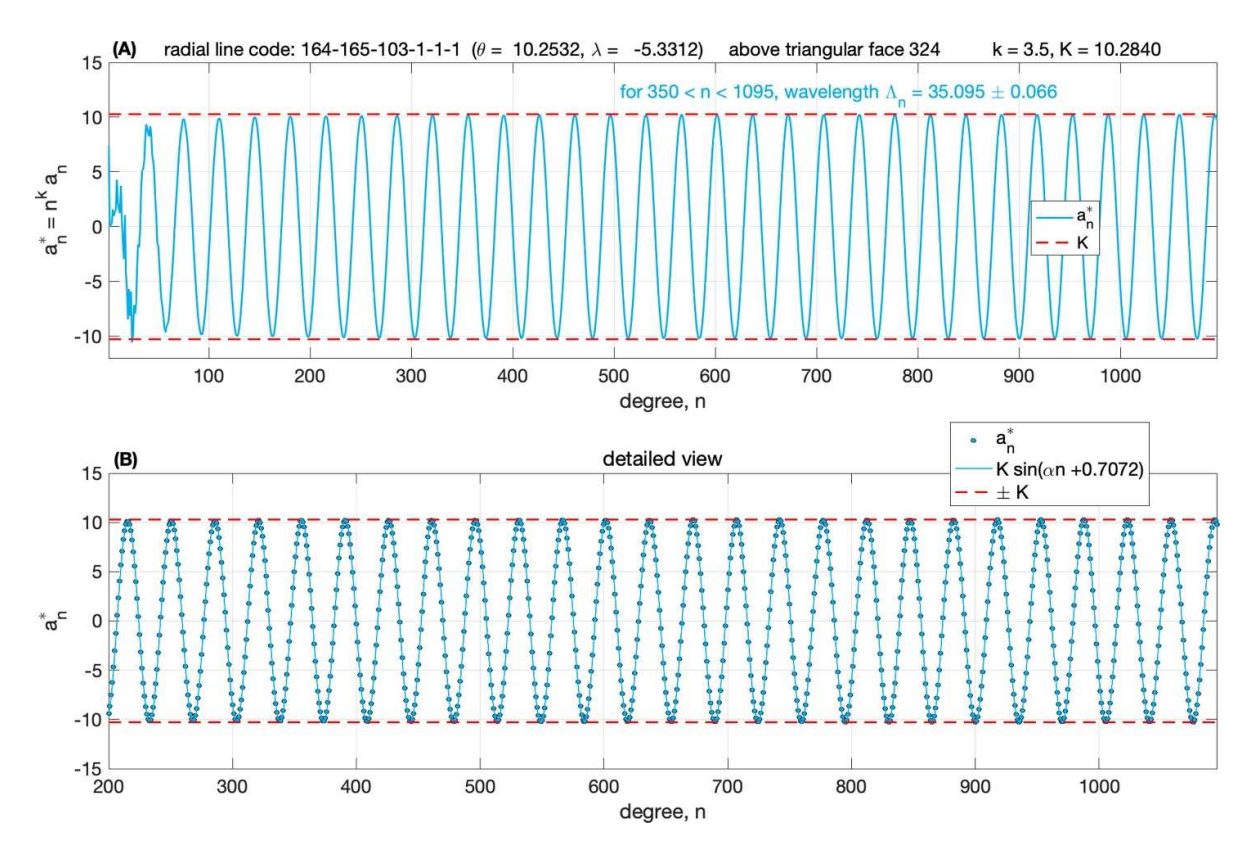


Figure 16. The behavior of the Taylor series coefficients for V on the radial line through the centroid of face 324. (A) The scaled coefficients $a_n^* = n^k a_n$ versus degree, n. Note that asymptotic behavior seems well established when n > 200 provided that k = 7/2. (B) In this plot, the coefficients are represented by the dots, and the oscillating curve is $K \sin(\alpha n + \beta_a)$, where K = 10.284, $\alpha = \theta$ is the angle between this radial line and the singular radial line (figure 2), n is treated as a continuous real variable, and β is the phase angle (for this radial line) determined by weighted least-squares estimation. In this plot and all similar plots, the estimated value of β is stated in the legend. In this case, $\beta_a = 0.7072$.

singular radial line (figure 2). It did not take long to realize that

$$a_n^* \simeq K \sin{(\alpha n + \beta_a)},$$
 (19)

where, as before, the symbol \simeq means that $a_n^* \to K\sin(\alpha n + \beta_a)$ as $n \to \infty$. The value of phase angle β_a depends on the particular radial line. Note that the symbol \simeq is sometimes interpreted as 'approximately equal to' (\approx) for 'large enough' n. This characterization, sometimes referred to as the 'asymptotic approximation,' depends as much on one's tolerance of error as it does on the actual behavior of the coefficients, and thus it is somewhat subjective.

We illustrate this asymptotic behavior by treating n as a continuous real variable and evaluating the sinusoid on the right-hand side of equation (19) at an interval $\delta n < 0.1$. This sinusoid is plotted as the continuous curve in figure 16(B), and the discrete values of a_n^* , for integer n, are plotted as small circles on top of this curve, so that it is easy to determine the level of agreement. For most practical purposes, the asymptotic approximation will be acceptable (for this radial line) when n > 200, and perhaps even earlier.

Next we examine the asymptotic bounds of the scaled errors $e_N^* = N^b e_N$ at the intersection of the same radial line and the Brillouin sphere, where R/r = 1 (figure 17). We find that

b=7/2, meaning that b=k, as for the cubic planet. We estimated the wavelength of the oscillation seen in figure 17(A), and found that $\Lambda \approx 35.1$, which is what we found for the oscillating coefficients in figure 16. The suggestion is that the asymptotic behavior of oscillations in prediction error on the Brillouin sphere can be described as

$$e_N^* \simeq B \sin(\alpha N + \beta_e),$$
 (20)

which is very similar to the asymptotic relation equation (19). We find that this asymptotic formula holds for every other radial line we have examined that is not parallel to the singular radial line. We test asymptotic equation (20) in figure 17(B), using the same approach that we used for the coefficients. The wavelengths seen in figures 16 and 17 are identical because both figures focus on the same radial line, and therefore have the same value of α . But note that the values of the phase angle β are different. That is, $\beta_a \neq \beta_e$ on the same radial line.

We now switch our focus to the radial line passing through vertex 141 (figure 14), where $\alpha = 44.8216^{\circ}$, about 4.37 times larger than the value of α for the radial line we have just examined. We show the results from our search for k and k in figure 18, and the results from our search for k and k in figure 19. We see that k = 1/2, as before, and that the

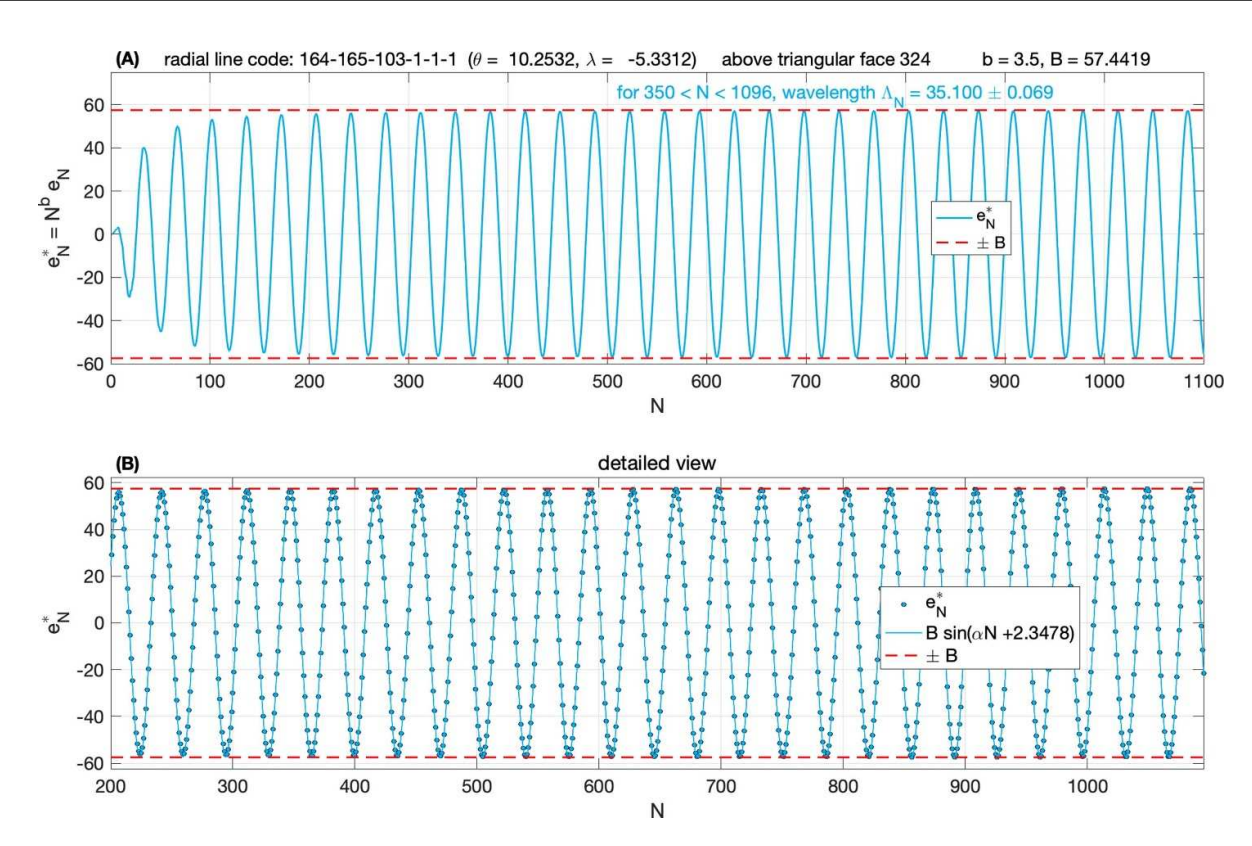


Figure 17. The behavior of the series prediction error for V on the radial line through the centroid of face 324. (A) The scaled errors $e_N^* = N^k e_N$ are plotted as a function of the truncation degree, N. (B) In this plot, the scaled errors are represented by the dots, and the oscillating curve is $B \sin{(\alpha N + \beta_e)}$, where B = 57.4419, $\alpha = \theta$ is the angle between this radial line and the singular radial line (figure 2), N is treated as a continuous real variable, and β_e is the phase angle (for this radial line) determined by a weighted least squares analysis. In this case, $\beta_e = 2.3478$ radians.

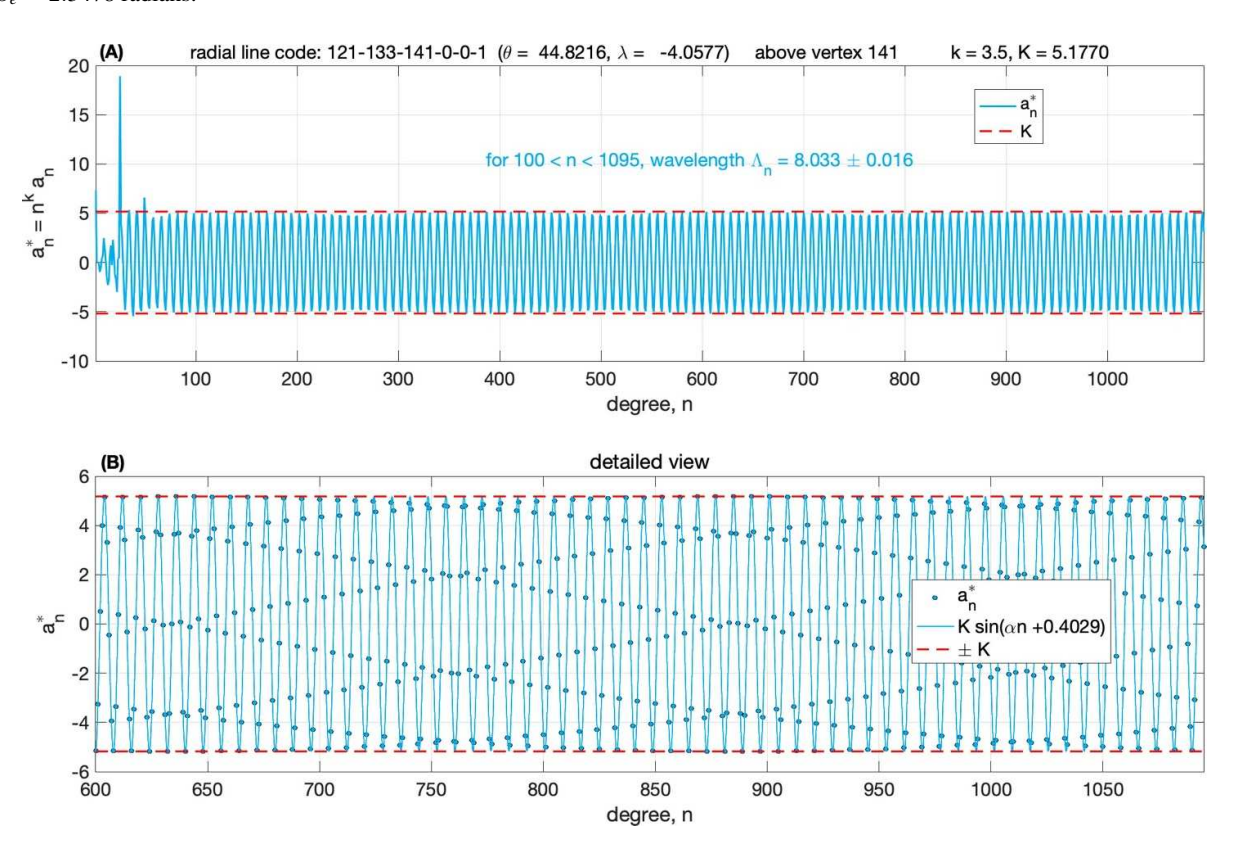


Figure 18. The behavior of the scaled Taylor series coefficients for V on the radial line through vertex 141. The format of parts (A) and (B) in this figure are the same as for parts (A) and (B) of figure 16. The parameter k = 7/2, as before. For this radial line $\alpha = 44.8216^{\circ}$, so the scaled coefficients a_n^* oscillate about 4.37 times faster than in figure 16.

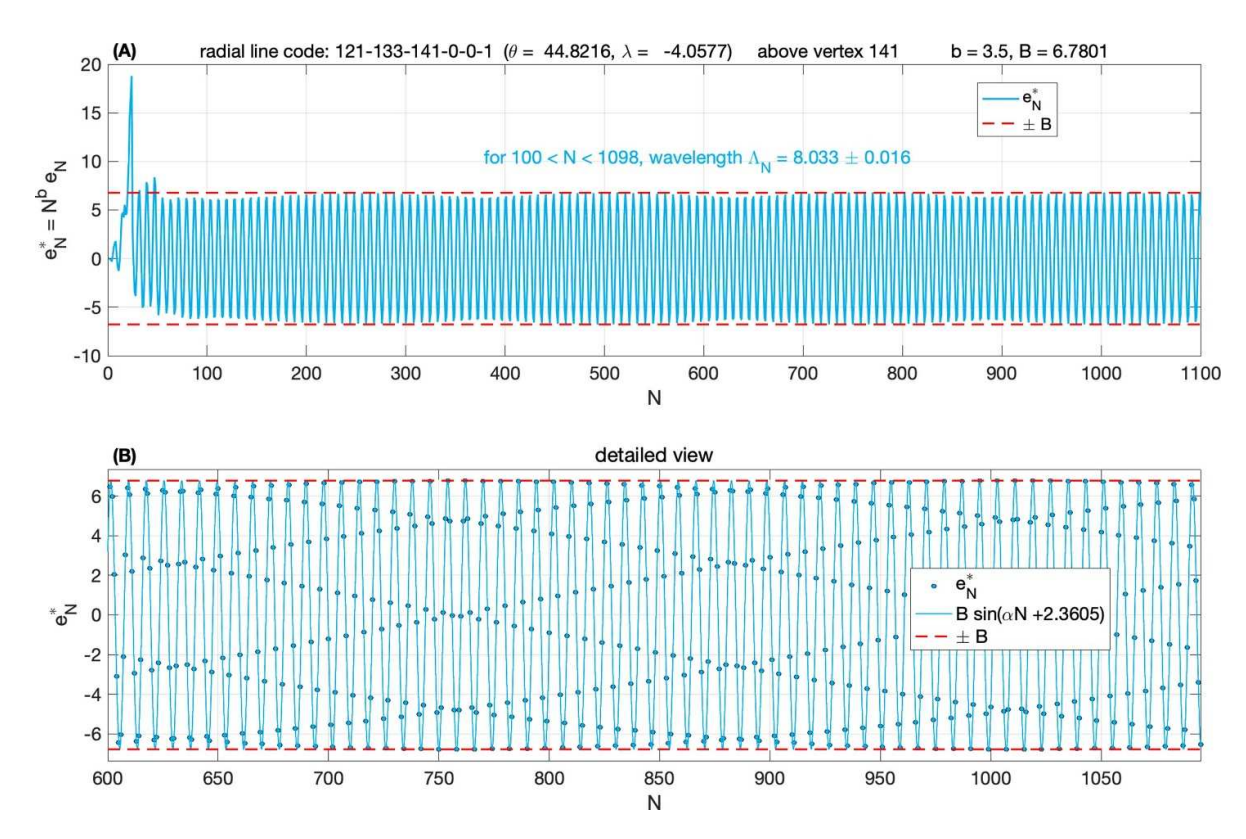


Figure 19. The behavior of the scaled prediction errors for V on the radial line through vertex 141. The format of parts (A) and (B) in this figure are the same as for parts (A) and (B) of figure 17. The parameter b = 7/2, as before. For this radial line $\alpha = 44.8216^{\circ}$, so the scaled coefficients e_n^* oscillate about 4.37 times faster than in figure 17.

scaled coefficients and scaled errors are oscillating at the same rate (and with the same wavelength) but about 4.37 times faster than for the previous radial line.

The asymptotic relationship equation (19) implies that rather special outcomes occur when $\alpha = 0$, on the singular axis, which passes through the highest vertex, and when $\alpha = \pi$, on the complementary radial line, which passes through the antipode. As $\alpha \to 0$, then $\Lambda \to \infty$, implying that, once asymptotic behavior is well established, the coefficients will never change their sign when $\alpha = 0$. This suggestion is verified in figure 20(A). Indeed, the coefficients do not change their sign for any value of n. The other remarkable finding is that k = 3 rather than 7/2. If we make a similar plot but with k = 2.9 or k = 3.1 we find no 'flattening' of the upper bound curve for the scaled coefficients for large values of n. Instead, the local upper bound on the scaled coefficients either strongly increases or strongly decreases with rising n.

Even when k = 3, the apparent 'convergence' of the scaled coefficients with the dashed red line, seen in figure 20(A), is misleading. Having found the appropriate value of k, we estimate the value of the asymptotic parameter K in plots of this kind by finding the largest absolute value of the scaled coefficients a_n^* after asymptotic behavior is well established, that is, ignoring the anomalous values that occur for small values of n. But in this case (figure 20(A)), the largest value of a_n^* is that for the largest value of n (figure 20(B)). We are surely underestimating the value of K. The convergence process is so slow on the singular radial line, we cannot reliably estimate the value

of *K*. The fact that the coefficients never change sign helps to explain this. Alternating signs (even with a long wavelength) encourages convergence of the series (section 5.2).

The other special case of interest is for the complementary radial line, with $\alpha=\pi$, where the oscillation of the scaled coefficients has a wavelength $\Lambda_n=2\pi/\alpha=2$, implying that the coefficient's signs will eventually alternate, strictly, from one value of n to the next. This expectation is confirmed in figure 21. For the second time we find that k=3. This anomalous value of k applies to the entire singular axis, that is, to the singular radial line and its complement. But in this case, convergence with the expected asymptotic behavior (equation (19)) is essentially complete when n exceeds about 250. This means that a_n^* very closely approximates $\pm K$. Such rapid convergence is promoted when the sign of the coefficients strictly alternates from one value of n to the next.

We cannot examine prediction error beneath the Brillouin sphere on the singular radial line, because there is no free space there, only the solid planet. But we can examine prediction error at the intersection of the singular radial line and the Brillouin sphere, that is, where the highest mountain's summit touches that sphere. We employ a trick to work around the fact that the Werner method can compute V above the surface of the polyhedral planet, but not on it. We compute V at a point on the singular radial line at $r = R + \epsilon$, and set $\epsilon \approx 10^{-400}$, so that the difference between V(R) and $V(R + \epsilon)$ is entirely negligible. This leads us to the scaled error plot figure 22, showing that b = 2 rather than the usual value of b = 7/2.

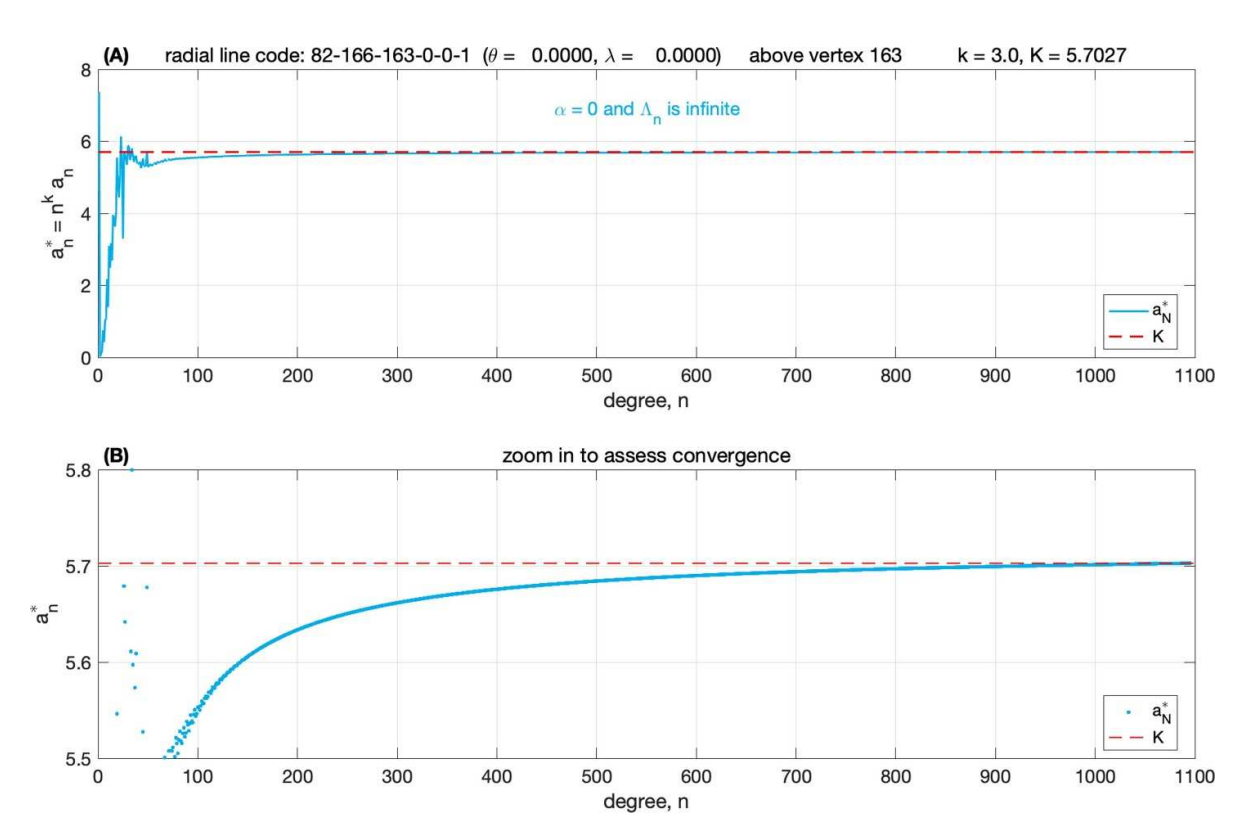


Figure 20. The behavior of the scaled Tayor series coefficients for V on the singular radial line through vertex 163, which lies on the Brillouin sphere.

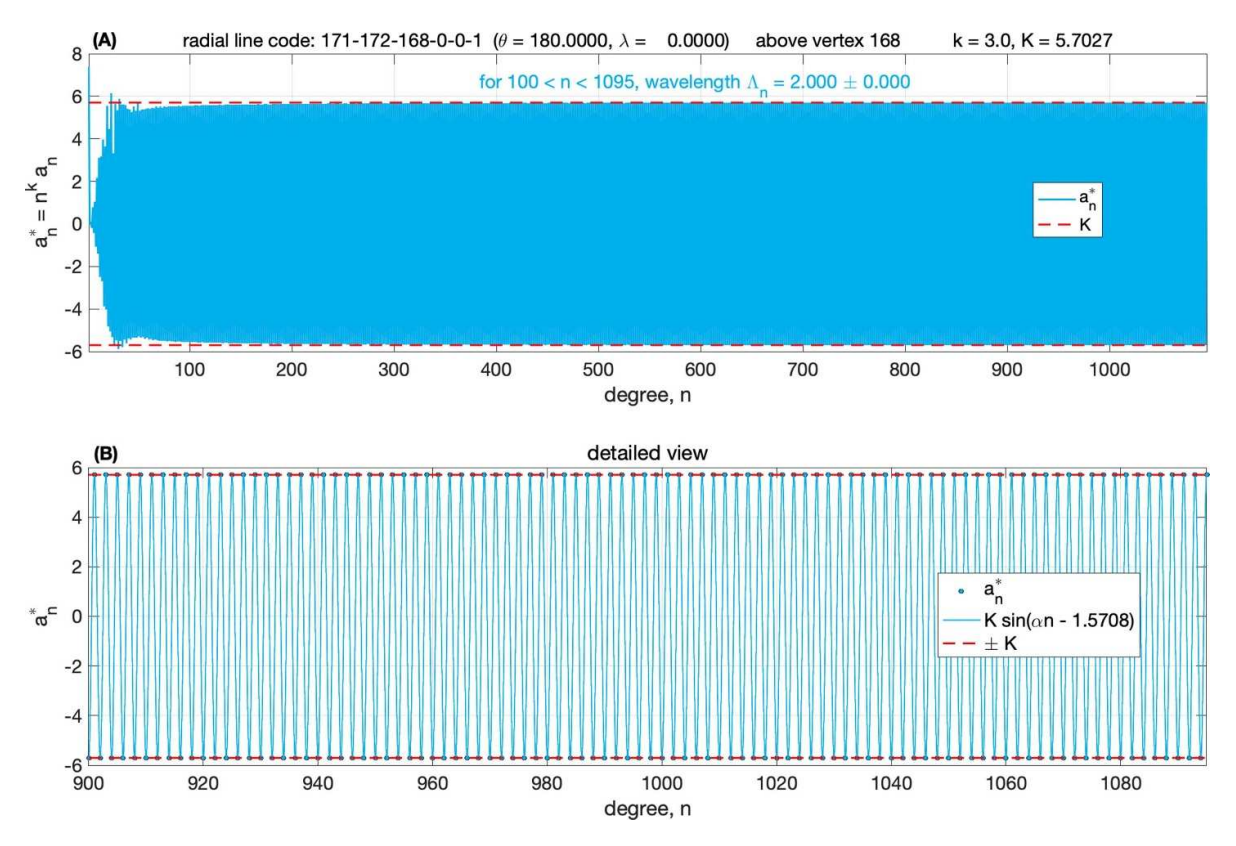


Figure 21. The behavior of the scaled Taylor series coefficients for V on the radial line through vertex 168, which is antipodal to the singular radial line. Note that in (B), the a_n^* have values very close to +K or -K, and they are strictly alternating in sign.

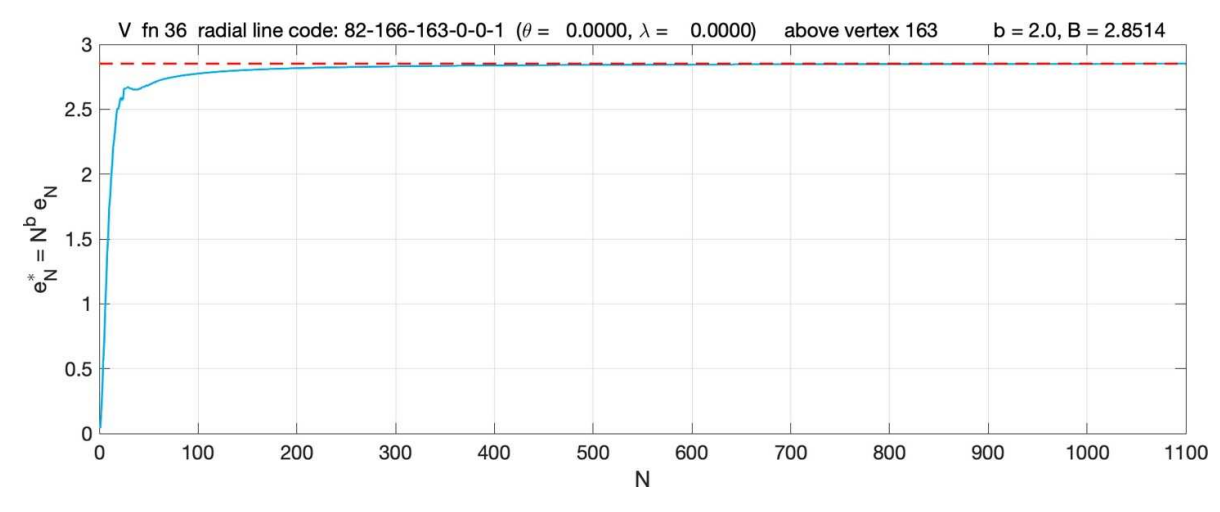


Figure 22. The behavior of the scaled prediction errors for V at the intersection of the Brillouin sphere and the singular radial line (that is, on vertex 163). We find that b = 2.

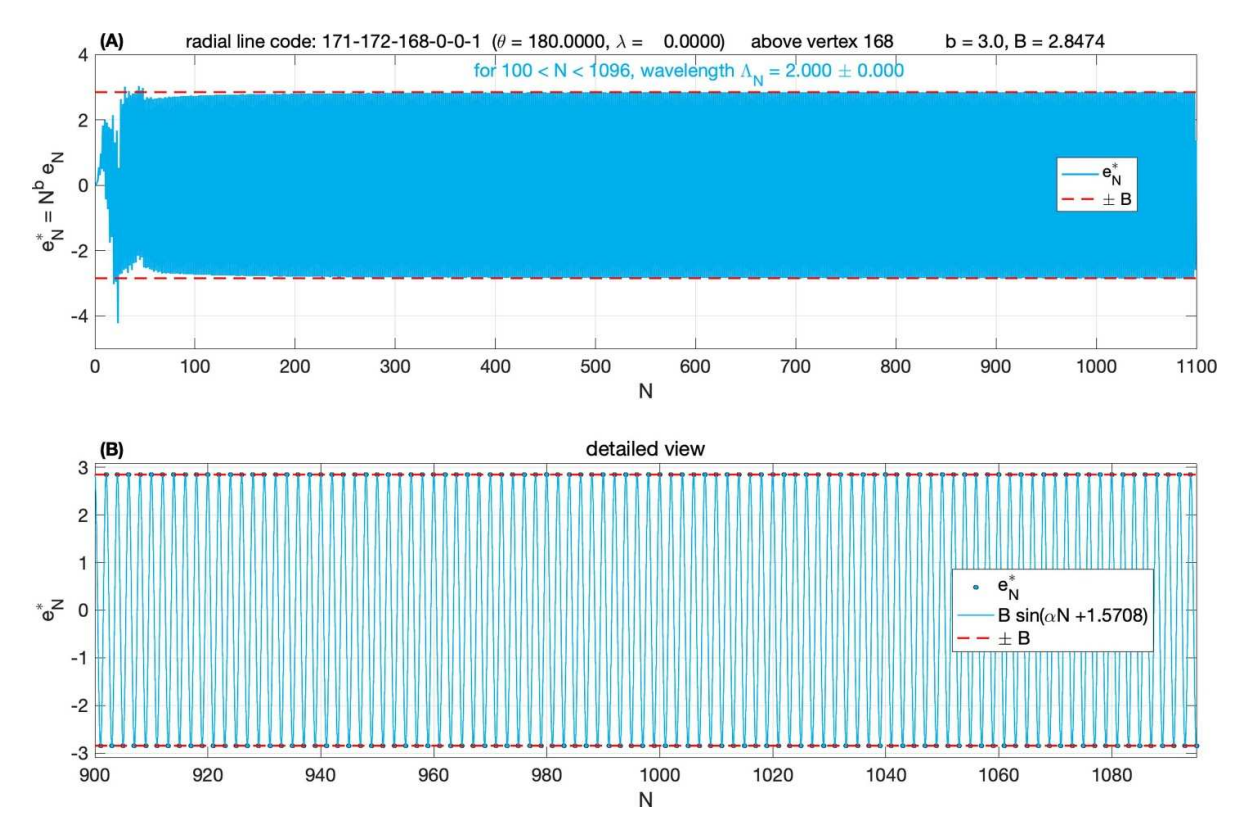


Figure 23. The behavior of the scaled prediction errors for V at the intersection of the Brillouin sphere and the radial line through vertex 168, which is antipodal to the singular radial line. Note that in (B), the e_N^* have values very close to +B or -B, and they are strictly alternating in sign.

There is free space both on and beneath the Brillouin sphere on the complementary radial line which passes through vertex 168. We examine the asymptotic behavior of the scaled series prediction errors e_N^* versus N in figure 23. We find that b=3 rather than the usual value of 7/2.

We conclude that, for this polyhedral planet, the asymptotic decay parameters for V are b=k=7/2 when $0<\alpha<\pi$. When $\alpha=0$ then k=3 and b=2, and when $\alpha=\pi$ then k=b=3. The singular radial line is the only radial line on which $b\neq k$.

This 'spatial quantization' of the asymptotic scaling parameters k and b provides additional support to an asymptotic theory of divergence and prediction error that is so strongly tied to the Brillouin sphere, and is frequently focused on what happens near the singular point on this sphere, where it touches the planet (Costin *et al* 2022).

While the presence and amplitude of topography does not affect the value of the asymptotic parameters k and b away from the singular axis, nor does it change the asymptotic behavior expressed by equations (19) and (20), it

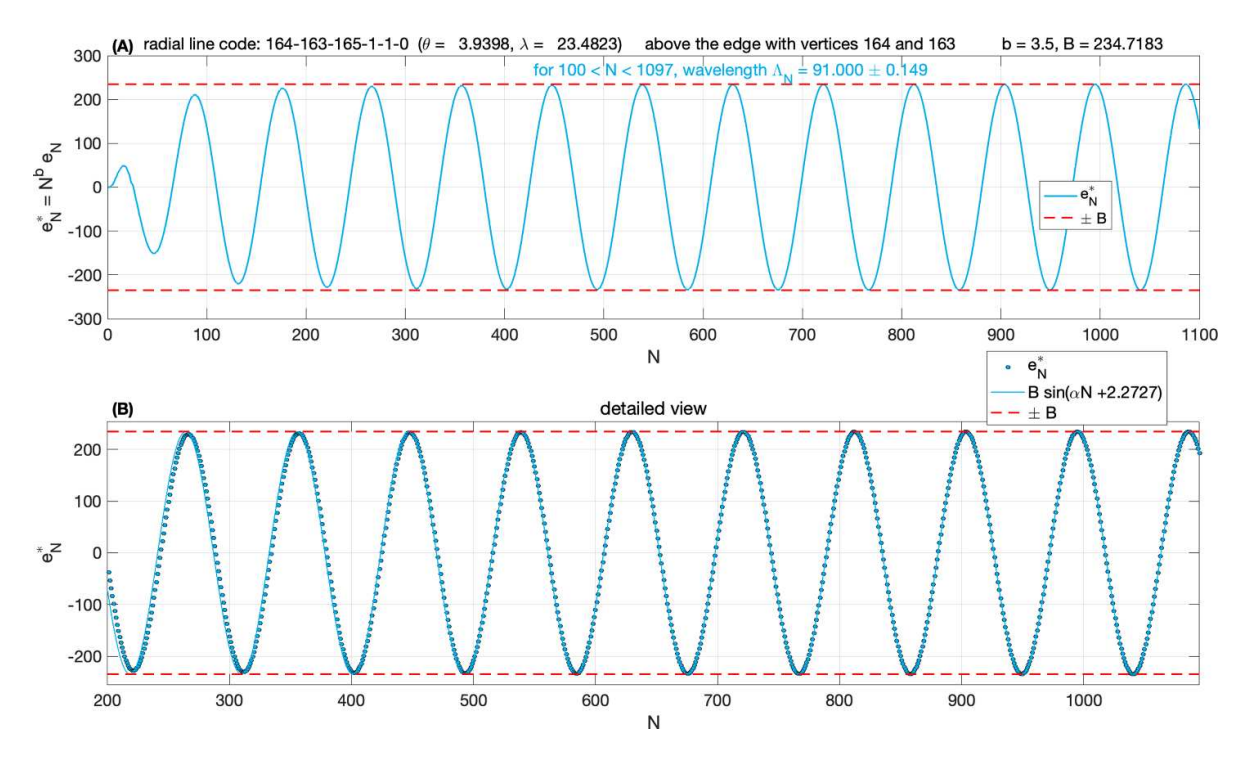


Figure 24. The behavior of the scaled prediction errors for V on the Brillouin sphere above the midpoint of the edge between vertices 164 and 163, where $\alpha = 3.94^{\circ}$. Notice in subplot (B) that there is a small but discernible offset between the e_N^* and the continuous curve representing asymptotic behavior (equation (20)), until N is about 700.

certainly does affect the parameters K and B, and also the rate of convergence towards asymptotic behavior. For example, if we search for k and b above a point in the middle of one the edges of the highest mountain, halfway between vertices 164 and 163, we find that K = 16.25 and B = 234.72, much higher values than we have seen so far. Furthermore, a careful visual inspection of figure 24(B) reveals that asymptotic behavior is not very well established until $N \approx 700$.

Even closer to the highest summit vertex, there are radial lines on which B > 500 ensures much larger prediction errors for V than prevail over nearly all the sphere.

7.4. Prediction error for V beneath the Brillouin sphere

We now show that Costin's formula, equation (13), correctly bounds the directly computed series prediction error for V beneath the Brillouin sphere. Rather than plot the errors $e_N = (V - V_N)$ versus N, we plot the absolute value of relative prediction error $e_N/V = (V - V_N)/V$ versus N. The upper bound should be E_N/V . We confirm this for the radial line passing through vertex 141, for four different values of r/R, in figure 25. Note that $N_{\rm opt} = 1748$ when r = 0.998R, but much deeper beneath the Brillouin sphere, at r = 0.96R, the impact of divergence manifests far more quickly, and $N_{\rm opt} = 86$. In this setting, relative error is greater than 1 when $N \sim 500$, meaning that the prediction V_{500} has no significant digits.

7.5. Bounding series coefficients and prediction error for g

We now consider asymptotic behavior in the TS coefficients for g_r . We do this for the radial line passing through vertex 141 in figure 26. As with the cubic planet, we find k = 5/2 when focusing on gravitational acceleration rather than gravitational potential. Note that the oscillations in the scaled coefficients follow the same asymptotic relationship, equation (19), seen previously with the coefficients for V. The wavelength Λ_n estimated in figure 26(A) is found by counting peaks, whereas in figure 26(B) the continuous sinusoid is generated by setting the wavelength to its asymptotic value $\Lambda_n = 2\pi/\alpha$ and simply estimating the sinusoid's phase angle using weighted least-squares estimation. Compare figure 26(B) with figure 18(B).

When we search for asymptotic bounds in the scaled series prediction error e_N^* for g_r , at the intersection of this radial line and the Brillouin sphere, then, unsurprisingly, we find b=5/2. The oscillations in e_N^* conform with the asymptotic relation equation (20), and the asymptotic wavelength $\Lambda_N=\Lambda_n=2\pi/\alpha$.

In the interests of brevity, we summarize, without illustration, the results of performing investigations on other radial lines, including all those depicted in figures 14 and 15: that $b^g = 5/2$ everywhere, no matter if the radial line passes through a vertex, a face or an edge, *except* for the singular radial line (with $\alpha = 0$), where $k^g = 2$ and $b^g = 1$, and the complementary radial line, (with $\alpha = \pi$) where $k^g = b^g = 2$.

It is possible to verify that, once we have estimated the value of *B* on the Brillouin sphere, Costin's formula bounds

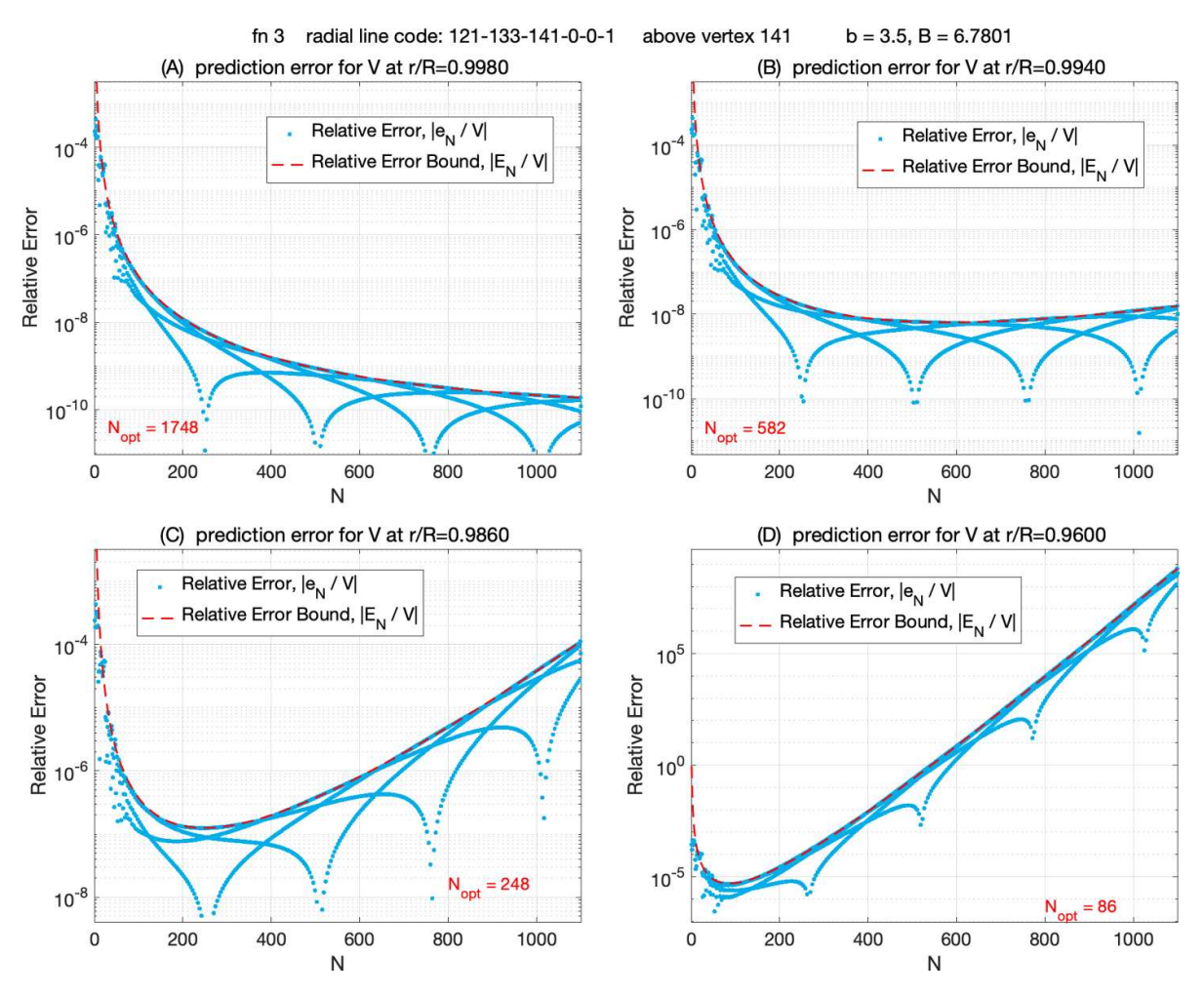


Figure 25. A comparison of the absolute value of the directly computed relative prediction error, $e_N/V = (V_N - V)/V$, and its asymptotic bound, E_N/V , from Costin's formula, equation (13), for a radial line passing through vertex 141. This comparison is made at four different depths beneath the Brillouin sphere: (A) r/R = 0.998, (B) r/R = 0.994, (C) r/R = 0.986, and (D) r/R = 0.96. Note that we plot the absolute values of relative error, since we are using a logarithmic scale. Also shown in each plot is the value of N_{opt} computed from equation (15).

the prediction error for g_r at any value of R/r. If we divide the observed prediction error and Costin's formula by the correct value for g_r , we can use Costin's formula to bound relative prediction error as well (figure 27).

76. Relationships between the parameters K and B in the asymptotic formulas for V and g

The asymptotic formulas equations (13) and (16) involve positive constants B and K, respectively. When these formulas are applied to the gravitational potential V or to the radial component of gravitational acceleration $g_r = \partial V/\partial r$, then we sometimes refer to them as B^V and K^V or B^g and K^g , respectively. In our treatment of the cubic planet (section 6), we noticed that $K^V/K^g \approx B^V/B^g \approx R$, and that $K^V/B^V \approx K^g/B^g$, on the radial line corresponding to the positive Z-axis. We find similar relationships for the polyhedral planet for many different radial lines, including those depicted in figures 14 and 15, and additional radial lines passing through the edges between adjoining triangular faces, and radial lines passing through a face composing one of the flanks of the highest mountain, at locations between the centroid of this face and the summit vertex, 163.

In appendix A, we prove, for any radial line with angle α in the open interval $0 < \alpha < \pi$, which excludes the singular radial line and its complement, that

$$\frac{K^V}{R^V} = 2\sin\alpha/2,\tag{21}$$

and if we combine this result with a result proven in appendix B, it follows that

$$\frac{K^V}{B^V} = \frac{K^g}{B^g} = 2\sin\alpha/2. \tag{22}$$

This equality applies to the ratios of true values of the asymptotic constants B^V , K^V , B^g , and K^g . In our numerical experiments for the polyhedral planet we estimate the values of these constants for various radial lines, and expect the estimates to lie very close to the true values, so we expect the ratios of our estimates to approximate the predictions of equation (22). We validate this expectation empirically in figure 28—see the black curve and the overlying data points for radial lines with differing values of α .

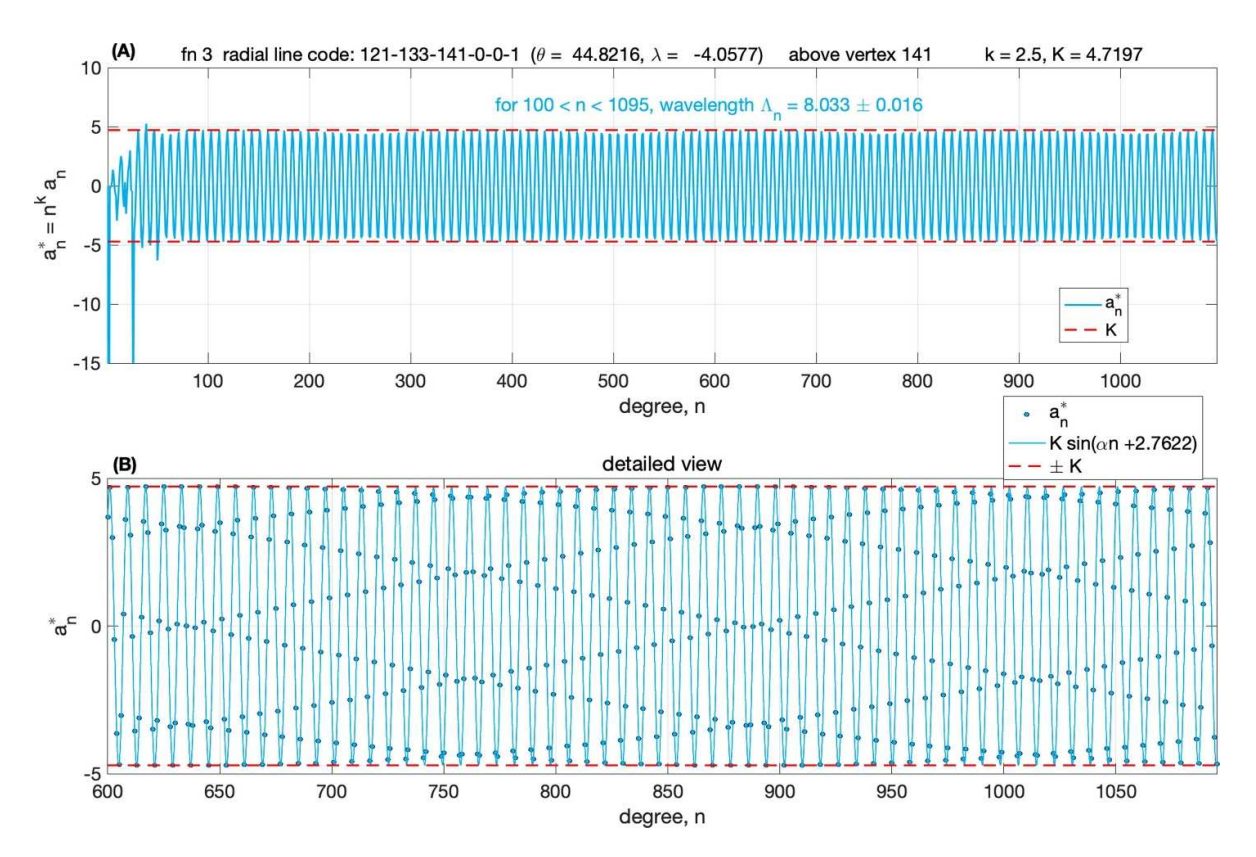


Figure 26. The behavior of the scaled Taylor series coefficients for $g_r = \partial V/\partial r$ on the radial line through vertex 141. The asymptotic behavior is evident only when we set k = 5/2.

When $\alpha=0$ then equation (22) does not apply, but we can prove that $K^V/B^V=b^V=2$ and $K^g/B^g=b^g=1$. This assertion is supported by our estimates for k^V and b^V on the singular radial line, which are 5.7027 and 2.8514, respectively, and by our estimates for k^g and b^g on the singular radial line, which both equal to 5.1938.

Our proof of equation (22) was limited to radial lines with angles α in the interval $0 < \alpha < \pi$, which excludes the radial line with $\alpha = \pi$. But we find that the predictions of equation (22) are close to the observed results when $\alpha = \pi$.

In appendix B, we prove that for any radial line with angle α (figure 2) in the range $0 < \alpha \le \pi$, or, in other words, for any radial line other than the singular radial line

$$\frac{B^V}{B^g} = \frac{K^V}{K^g} = R. \tag{23}$$

Again, this equality applies to the ratios of the true values of the asymptotic constants B^V , K^V , B^g , and K^g . In our numerical experiments for the polyhedral planet we estimate the values of these constants for various radial lines, and expect the estimates to lie very close to the true values (except in the case of the singular radial axis), so we expect the ratios of our estimates to approximate the predictions of equation (23). We validate this expectation empirically in figure 28—see the horizontal red line and the overlying data points for radial lines with differing values of α .

Our proof of equation (23) excluded the singular radial line, with $\alpha = 0$, but we find that in this special case $K^V/K^g = R$ and $B^V/B^g = R/2$.

8. Discussion

We begin this discussion by summarizing in table 1 how the asymptotic decay constants k and b vary with the angle α when we describe the asymptotic behavior associated with the TS coefficients, equation (16), and series prediction error, equation (13), either for potential, V, or for the radial component of gravitational acceleration, g_r . The spatial quantization of these decay constants is remarkable. The value of the constants on the singular axis—that is, on the singular radial line (with $\alpha=0$) or on the complementary radial line (with $\alpha=0$) differ from the values for every other radial line. Despite this spatial quantization, $k^g=k^V-1$ and $b^g=b^V-1$ everywhere. The practical consequence of this is that the impacts of divergence beneath the Brillouin sphere tend to be worse for g_r than for V at the same location (compare, for example, figure 25 with figure 27).

There is a similarly abrupt change in the behavior of the various ratios of the asymptotic scale constants K and B for V and g_r , as seen in table 2.

Note that when $\alpha = \pi$, then $2 \sin \alpha/2 = 2$, so that $K^V/B^V = 2$ both on the singular radial line and on its complementary radial line, though the same is not true for the ratio K^g/B^g . So 'anomalous' behavior for these ratios is confined to the singular radial line ($\alpha = 0$), and not the entire singular axis ($\alpha = 0$ or $\alpha = \pi$).

To simplify this discussion, let us exclude the singular axis, and focus on the rest of the planet (where $0 < \alpha < \pi$), where $k^V = b^V = 7/2$, $k^g = b^g = 5/2$, $K^V/K^g = B^V/B^g = R$ (where R)

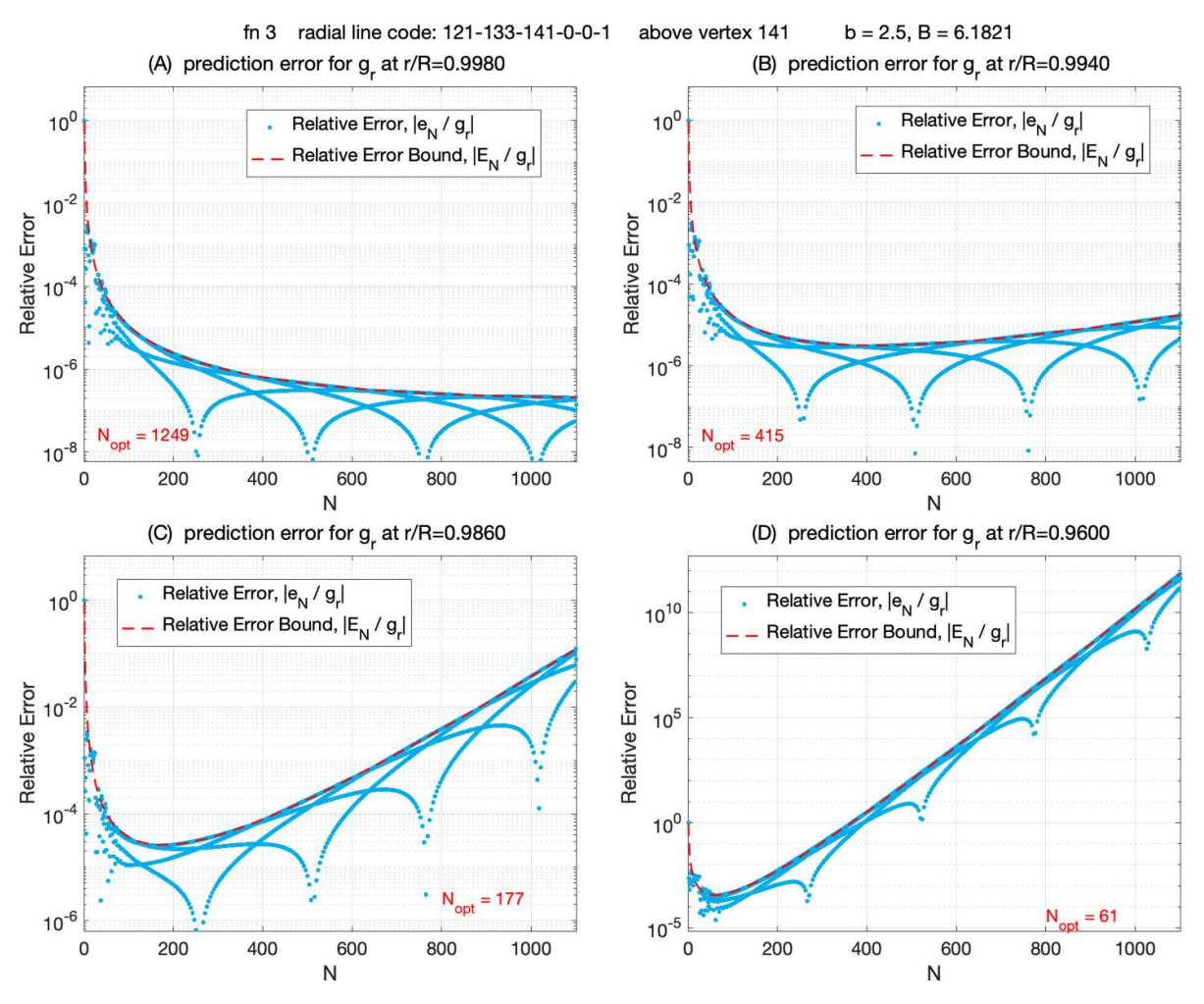


Figure 27. The absolute value of the relative prediction error for $g_r = \partial V/\partial r$ on the radial line through vertex 141 for four values of r/R, and the upper bound predicted using the Costin formula. Compare this plot with figure 25 for potential, V, where the four values of r/R are the same as those in (A)–(D) above.

is the radius of the Brillouin sphere), and $K^V/B^V = K^g/B^g = 2\sin\alpha/2$. These identities are extremely useful. For example, the last identity implies that

$$B^V = K^V / (2\sin\alpha/2), \qquad (24)$$

which allows us to compute B^V from K^V . So, we can bound the prediction errors for V on a radial line from a quantity (K^V) that we can derive directly from the TS coefficients for V on that line. Crucially, equation (24) enables us to bound series prediction error for V without the need to accurately compute the true value of V! Furthermore, since $B^g = B^V/R$ then

$$B^g = K^V / (2R\sin\alpha/2). \tag{25}$$

This means we can bound the prediction errors for g_r from the TS coefficients for V on the relevant radial line, without the need to accurately compute the true value of g_r .

Because we can compute the true values of V and g_r for our polygonal planet with very high numerical precision, we have been able to confirm Costin's formula, equation (13), bounding series prediction error. We discovered a similar formula, equation (16), that bounds the absolute values of the

TS coefficients on a given radial line, which, though it was not isolated or discussed by Costin *et al* (2022), is implicit in their analysis. Indeed the asymptotic behavior in the TS coefficients underpins the asymptotic behavior in the series prediction error on the same radial line, both for V and for g_r .

Our numerical experiments with TS coefficients and prediction error led us to two new asymptotic relationships: equation (19), describing how scaled TS coefficients a_n^* oscillate as degree n increases, and equation (20), describing the rate of oscillation of the scaled errors (e_N^*) as truncation degree N increases. Of course, the original (unscaled) coefficients a_n oscillate with the same frequency as the scaled coefficients, and the unscaled errors e_N oscillate with the same frequency as the scaled errors, but these oscillations are harder to perceive graphically when the scaling is not present to remove the strong decay envelopes that characterize the unscaled quantities. The rate of oscillation for the coefficients and the prediction errors depend on the angle α for the radial line of interest, and, as a result, the coefficients and the errors oscillate on the same radial line with the same wavelength (Λ_n = $\Lambda_N = 2\pi/\alpha$). Consistent with this result, we have seen that the TS coefficients for V and g_r on the singular radial line (with

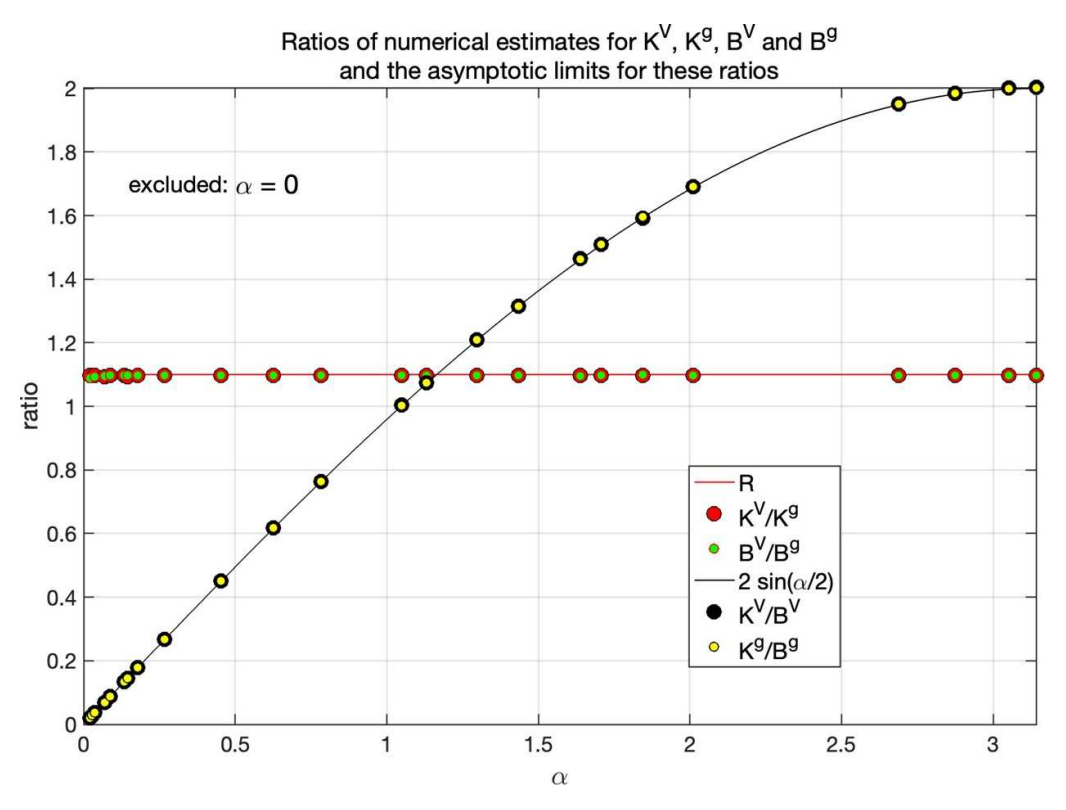


Figure 28. The theoretical expressions for the ratios between B^V , K^V , B^g , and K^g , and the observed ratios estimated for the radial lines depicted in figures 14 and 15, plus some additional radial lines, with various values of α , but excluding the singular radial line (with $\alpha = 0$).

Table 1. The asymptotic decay constants for the polyhedral planet as a function of the value of the angle α for the radial line of interest.

α	k^V	b^V	k^g	b^g
$0 \\ 0 < \alpha < \pi$	3 7/2	2 7/2	2 5/2	1 5/2
π	3	3	2	2

Table 2. The ratios of the asymptotic constants B^V , K^V , B^g , K^g for the polyhedral planet as a function of the angle α for the radial line of interest.

α	K^V/K^g	B^V/B^g	K^V/B^V	K^g/B^g
0	R	R/2	2	1
$0 < \alpha < \pi$	R	R	$2\sin\alpha/2$	$2\sin\alpha/2$
π	R	R	$2\sin\alpha/2$	$2\sin\alpha/2$

 $\alpha=0$) do not oscillate at all, but maintain a constant sign, which greatly slows the rate of convergence of these series. By way of contrast, the coefficients are strictly oscillating on the complementary radial line (with $\alpha=\pi$), meaning that the sign of a_n changes every time that $n \to n+1$.

The traditional view of SH series models for the gravitational potential, V_N , truncated at degree and order N, is that their prediction errors arise from errors of omission (the impact of truncation at degree N) and errors of commission (e.g. procedural shortcomings in downward continuation or in

the least-squares methodology used to solve for the SH coefficients). Series truncation limits the adjustable degrees of freedom and the spatial resolution of the SH series, and thus limits the ability of the model to 'follow' the actual variations of V, especially in high and rough mountain belts. In this traditional view, the prediction errors associated with limited spatial resolution could be reduced by increasing the truncation degree N, provided that the gravitational data set is sufficient to support the inversion for an increased number of SH coefficients. However, we have seen that this notion is not really true. Even if we had larger and higher quality data sets, once N increases beyond some critical value, $N_{\rm opt}$, prediction errors will get worse as N increases further, because the increase in prediction error due to intensifying divergence overwhelms any reduction in prediction error due to improved resolution. For $N \gg N_{\rm opt}$, prediction error tends to increase exponentially with increasing N. One of the key findings of this work is, for our polygonal planet, the optimal truncation degree varies by factors greater than 20, depending on the location in free-space beneath the Brillouin sphere (e.g. figures 25 and 27), for SH models of V and g_r .

There is no globally optimal value for N_{opt} .

Divergence rates and prediction errors in free space vary 'laterally,' when latitude and longitude change, but the radial coordinate r does not. These lateral changes are encoded by changes in the asymptotic scale factor, B, which also reflects how the TS coefficients change as the radial line tilts. But divergence and prediction error typically intensify much more rapidly as depth beneath the Brillouin sphere increases.

Indeed, series prediction error varies very nearly exponentially with depth d=R-r (for r < R). The logarithm of the upper bound on prediction error, E_N , is actually proportional to the quotient d/R (equation (14)). The maximum depth, $d_{\rm max}$, we can achieve in free space depends on the topography of the planet. If we compare the topography of Earth and the Moon, we see that d/R achieves significantly larger near-surface values on the Moon. For example, the total radial relief of the Moon, $(r_{\rm max}-r_{\rm min}=d_{\rm max})$, expressed as a fraction of the radius, R, of the Brillouin sphere of the Moon, is much larger than the same statistic for the Earth.

The problem of SHE divergence beneath the Brillouin sphere is a fundamental problem. Any representation of the external gravitational potential derived directly from equation (2) will be flawed beneath the Brillouin sphere, and the closer we get to the surface, the more severe these flaws become. The problem for physical geodesists building gravitational models for the Earth and other planets using SH series is not that Laplace's equation $(\nabla^2 V = 0)$ is not valid beneath the Brillouin sphere—it is valid everywhere in free space—but rather that a very high degree SH series, equation (4), is not an optimal representation of the gravitational potential anywhere beneath the Brillouin sphere. The magnitude of divergencedriven prediction errors depends on the values of the asymptotic constants k, K, b, and B, and these depend on the morphology of the planet. In a future paper we will address the scale of this problem for planets which are more similar, in terms of size, mass and topography, to the Earth and our Moon.

The Earth Gravitational Model 2008 (EGM2008) for V is expressed using SH coefficients complete through degree and order 2159, with additional coefficients up to degree 2190 and order 2159 (Pavlis et al 2012). Although EGM2008 poses as a SH series, it is actually an ellipsoidal harmonic series whose coefficients have been transformed into SH coefficients using the Hotine-Jekeli transformation due to Jekeli (1988). (The 'missing' orders in the degree range 2160-2190, are a natural consequence of using this transformation). The least-squares problem used to estimate the coefficients of EGM2008 was posed on a reference ellipsoid closely corresponding to sea level. This ellipsoid of rotation has its center at the Earth's center of mass, its semi-minor axis lies on the Z-axis, and its semi-major and semi-minor axis lengths are $a \approx 6378.14$ km and $b \approx 6356.75 \,\mathrm{km}$, respectively. The radius of the Earth's Brillouin sphere $R = 6,384.415 \pm 0.030$ km. Thus, at the equator, the EGM reference ellipsoid lies about 6.3 km below the Earth's Brillouin sphere, and at the poles it lies about 27.7 km below the Earth's Brillouin sphere. The Hotine-Jekeli transformation delivers SH coefficients developed on the EGM reference sphere, whose radius is a, so that the equators of the reference sphere and reference ellipsoid coincide. The EGM reference sphere and the Brillouin sphere of the Earth have a common center, so the former underlies the latter at a constant depth of $(R-a) \approx 6.28$ km. The EGM reference sphere is the Brillouin sphere of the EGM reference ellipsoid, which is about 0.1% smaller than the Brillouin sphere of the Earth.

While use of the Hotine-Jekeli transformation and two reference surfaces complicates the discussion of divergence and prediction error, the fundamental representation problem remains—i.e. trying to represent a definite physical quantity with a locally divergent series. We will discuss EGM2008 in greater detail in a future paper.

Sprlák and Han (2021) utilized end-of-mission GRAIL satellite data, acquired below the Brillouin sphere of the Moon, to argue that the disagreement between these observations and the predictions of several global gravity models for the Moon (based on much larger quantities of GRAIL data acquired above the Brillouin sphere) implies that these SH series models manifest divergence beneath the Brillouin sphere. This is the first argument known to us, for divergence of the SHE beneath the Brillouin sphere, that is based on physical observations.

Understanding and mitigating the impact of the representation problem is of considerable practical significance. For example, global gravitational models are used to provide 'gravity compensation' for inertial navigation systems (INSs). As the accelerometers and the gyros incorporated into state-of-the-art INS units have improved, the accuracy of gravity compensation (that is taking account of spatial variations of gravity acceleration and, especially, the deflection of vertical) has emerged as a limiting factor for navigational accuracy, particularly in mountain belts.

Gravity compensation of a different kind is becoming a critical issue for conventional or quantum networks incorporating regional or global networks of atomic clocks. The fractional frequency instability, $\delta f/f$, of modern atomic clocks has been rapidly improving, and state-of-the-art systems now have an instrumental stability $|(\delta f/f)_{\text{instr}}| < 10^{-18}$ (McGrew *et al* 2018). Clock frequency shifts in response to changes in gravity potential, W. (The difference between gravity potential, W, and gravitational potential, V, is that the former is the sum of the latter and the potential associated with the centrifugal forces driven by Earth rotation). The gravitational red shift (or gravitational time dilation) driven by a difference or change in gravity potential, δW , is given by

$$\left(\frac{\delta f}{f}\right)_{\text{grav}} = -\frac{\delta W}{c^2},\tag{26}$$

where c is the speed of light. This equation implies that moving an atomic clock near the surface of the Earth downwards by about 1 cm causes that clock to slow down to the degree that $|(\delta f/f)_{\rm grav}| \ge |(\delta f/f)_{\rm instr}|$, meaning that the resulting change in clock frequency is already detectable, and—given the rather stunning rate of improvement of atomic clock technology in the last five years (Bothwell *et al* 2022)—will soon be *easily* detectable. It is not so much the clock that is slowing as it descends, but rather time itself is slowing down. Timing specialists working with networks of atomic clocks already make efforts to take into account the differences in W at the various clock locations, so they can compare or average their rates.

Consider the problem of providing a user in a conventional or a quantum network with a virtual atomic clock derived from an analysis of a distributed network of actual atomic clocks. That user's virtual clock must also account for gravitational time dilation at the user's location. This requires us to estimate *W* at that location with an accuracy comparable to the

change in W that occurs near the Earth's surface when position shifts vertically by about 1 cm (or less). Since the user could be located almost anywhere, it is likely that a global gravitational model will be used to predict V, and calculate W. (The uncertainty in W would be dominated by the uncertainty in V). The present-day reality is that we cannot predict V or W at the order of 1 cm-equivalent accuracy over most of the surface of the Earth, and in some areas we cannot get within a factor of 10 of that goal. And in the near future, atomic clocks will improve to the point that even this \sim 1 cm-equivalent goal will prove inadequate.

Improving global gravity models, so as to improve gravity compensation for INS and timing networks, is not just a matter of resolving the representation problem—instrumental errors are an issue too. Nevertheless, understanding and mitigating (or 'side-stepping') the representation problem is obviously an important part of ensuring that gravity compensation does not become the dominant factor limiting the performance of future geospatial technologies, including those focused on positioning, navigation and timing.

9. Concluding remarks

The ubiquity of divergence beneath the Brillouin sphere, and the inevitable consequence of model prediction error, suggests that the scientific community needs to find a way of representing the external potential field beneath the Brillouin sphere by means other than direct evaluation of a SH polynomial. Ultra-accurate simulations of the external gravity field, of the kind employed in this study, can provide guidance as we redesign the mathematical foundations of global gravity modeling. Moreover, these simulations can be extended to account for density variations within planets such as the Earth, and also represent topography more realistically. It is possible to build planetary models featuring variable (but piece-wise constant) density by linear superposition of suites of constant-density polyhedra, mostly nested one inside another like matryoshka or 'babushka' dolls. Such simulated planets will not allow us to escape the divergence problem for the outermost polyhedron at least. And if one solution in this linear suite involves a diverging series, then the superposition of all the elementary solutions will diverge too. The need for density layering, and the desirability of representing topography realistically, suggests that ultra-accurate simulations of the gravitational field for Earth-like or Moon-like planets will require polyhedra consisting of millions of triangles.

Data availability statement

No new data were created or analysed in this study.

Acknowledgment

We are grateful to three anonymous reviewers for their very valuable comments and suggestions.

Appendix. A

In this appendix we utilize the notation of Costin *et al* (2022). For example, the angle between the singular radial line and some other radial line of interest (figure 2) is represented by θ rather than by α . In this appendix, as in Costin *et al* (2022), α denotes the exponent of the Hölder condition. (This was used to characterize the continuity of planetary topography in an ϵ -neighborhood of the planet's highest point). In the last paragraph of this appendix, we will translate our key result (obtained below) back into the notation employed in the rest of this paper.

Our starting point is formula (23) in Costin *et al* (2022) giving the asymptotic behavior \tilde{C}_n of the SHE coefficients C_n . This formula states that for large n, the coefficients of the SHE series have the asymptotic form

$$C_{n} \approx \tilde{C}_{n} := \frac{R^{n+3}}{n^{\frac{3}{2} + \alpha + 1}} \frac{\sqrt{2} \Gamma(\alpha + 1)}{\sqrt{\pi}} \times \Re \left(e^{-i\pi/4} e^{i(n+1/2)\theta_{0}} \left[\left(i^{\alpha} \left[ig_{+} + g_{1}a_{+} \left(1 + \alpha \right) \right] - \left(-i \right)^{\alpha} \left[ig_{-} + g_{1}a_{-} \left(1 + \alpha \right) \right] \right) \right], \tag{27}$$

where α is the Hölder exponent and $\Re(z)$ denotes the real part of the complex number z.

This can be written in simplified form as

$$\tilde{C}_n = \Re \left[A e^{in\theta} n^{-\left(\frac{3}{2} + \alpha + 1\right)} \right], \tag{28}$$

where $A = A_1 + iA_2$ is the complex constant

$$A = \frac{i e^{-\frac{i}{4}\pi} e^{\frac{i}{2}\theta} \sqrt{2}}{\sqrt{\pi}} \left[(2a_{-} + 2a_{+}) g_{1} + i g_{+} + g_{-} \right].$$
 (29)

Note that the exponent of n in equation (28) is $-(\frac{3}{2} + \alpha + 1)$, and that $(\frac{3}{2} + \alpha + 1)$ corresponds to the positive constant k in equation (16) in the main text. We have already established that, for polygonal planets of constant density, k = 7/2 when $0 < \theta < \pi$, implying that $\alpha = 1$. In this case equation (28) becomes

$$\tilde{C}_n = \Re \left[A e^{in\theta} n^{-\frac{7}{2}} \right]. \tag{30}$$

The following proposition is based on the assumption that $0 < \theta < \pi$, so it does not apply to a radial line with $\theta = 0$ or $\theta = \pi$.

Proposition 1. Assume that $C_n = \tilde{C}_n[1 + \frac{c+o(1)}{n}]$ (this is the case for polyhedral planets of constant density). For R=1 and $\alpha=1$ we have that \tilde{C}_n satisfies (30), therefore \tilde{C}_n takes all the values in the interval $[-Kn^{-7/2}, Kn^{-7/2}]$ where $K=\sqrt{A_1^2+A_2^2}$, and the remainder $\sum_{k=n}^{\infty} C_k$ asymptotically takes all the values in the interval $[-Bn^{-7/2}, Bn^{-7/2}]$ where $B=\frac{K}{2\sin(\theta/2)}$ if, as generically the case is, θ is irrational; otherwise it takes a discrete set of values.

Proof of proposition 1

We estimate

$$R_{N} = \sum_{n=N}^{\infty} e^{in\theta} n^{-\frac{7}{2}} \left[1 + \frac{c + o(1)}{n} \right].$$
 (31)

Lemma 1. We have

$$R_N = -\frac{e^{iN\theta}}{e^{i\theta} - 1} N^{-7/2} + o\left(N^{-7/2}\right). \tag{32}$$

Proof. Noting that

$$\left| \sum_{n=N}^{\infty} e^{in\theta} n^{-\frac{7}{2}} \frac{1}{n} \right| < \text{Const.} N^{-\frac{7}{2}}$$

(by the integral test) to estimate R_N we can ignore the terms o(1) in (31).

Let

$$g(n) = \frac{1}{e^{i\theta} - 1} e^{in\theta} n^{-\beta} \left(1 + \frac{1}{n} \frac{\beta e^{i\theta}}{e^{i\theta} - 1} \right).$$

Using the binomial formula we have $(n+1)^{-\beta} = n^{-\beta} \left(1 + \frac{1}{n}\right)^{-\beta} = n^{-\beta} (1 - \frac{\beta}{n} + O(n^{-2}))$. Applying this, a straightforward calculation shows that

$$e^{in\theta}n^{-\beta} = g(n+1) - g(n) + O(n^{-\beta-2}),$$
 (33)

where $O(n^{-\beta-2})$ denotes a term bounded in absolute value by const $\cdot n^{-\beta-2}$.

We now sum (33) (where β is 7/2 or 9/2) and obtain

$$\sum_{n=N}^{\infty} e^{in\theta} n^{-\beta} = g(N+1) - g(N) + g(N+2) - g(N+1)$$

$$+\ldots+\sum_{n=N}^{\infty}O\left(n^{-\beta-2}\right)=-g\left(N\right)+O\left(n^{-\beta-1}\right),$$

where we used the integral test again to see that $\left|\sum_{n=N}^{\infty} O(n^{-\beta-2})\right| \leqslant \operatorname{const} \cdot n^{-\beta-1}$.

We obtain the estimate (32).

To finish the proof of proposition 1, note that while C_n has the asymptotic behavior (28), the remainder $\operatorname{Rem}_n := \sum_{k=n}^{\infty} C_k$ is, by lemma 1,

$$\begin{aligned} \operatorname{Rem}_{n} &= \Re[AR_{n}] \asymp \Re\left[A\frac{e^{in\theta}}{1 - e^{i\theta}}n^{-7/2}\right] \\ &= \Re\left[A\frac{e^{in\theta - i\theta/2}}{e^{-i\theta/2} - e^{i\theta/2}}n^{-7/2}\right] = \Re\left[A\frac{e^{in\theta - i\theta/2 + i\pi/2}}{2\sin\left(\theta/2\right)}n^{-7/2}\right] \\ &= \frac{1}{2\sin\left(\theta/2\right)} \Re\left[Ae^{in\theta - i\theta/2 + i\pi/2}n^{-7/2}\right], \end{aligned}$$

which proves proposition 1.

In this appendix, we have proven that $B = K/(2\sin(\theta/2))$ when $0 < \theta < \pi$. To translate this result into the notation of the main text, we must replace the symbol θ with the symbol α . So, if $0 < \alpha < \pi$ then $B = K/(2\sin(\alpha/2))$.

Appendix. B

Assume a radial line A has been fixed, with V^A the restriction of the potential function V to A and g_r^A the restriction of $\partial V/\partial r$ to A. Note that g_r^A may also be viewed as the restriction of g_r to A, where g_r is the radial component of $\mathbf{g} = \nabla(V)$.

Following (10) we may write the TS for V^A at $r = \infty$ as

$$TS\left(V^{A}\right)\left(z\right) = \sum_{m=1}^{\infty} b_{m} z^{m},\tag{35}$$

where z = z(r) = R/r.

Proposition 2. The Taylor series for g_r^A at $r = \infty$ is given by

$$TS\left(g_r^A\right)(z) = \sum_{m=2}^{\infty} c_m z^m,\tag{36}$$

where $c_{m+1} = -(m/R)b_m$ for $m \ge 1$.

Proof. One has

$$\frac{d}{dr}(z^m) = \frac{d}{dr}\left(\frac{R^m}{r^m}\right) = -mR^m r^{-(m+1)} = -m/R\left(\frac{R^{m+1}}{r^{m+1}}\right)$$

$$= -(m/R)(z^{m+1}).$$
(37)

Then

$$TS\left(g_r^A\right)(z) = \frac{d}{dr}\left(TS\left(V^A\right)(z)\right) = \sum_{m=1}^{\infty} b_m \frac{d}{dr}(z^m)$$
$$= \sum_{m=1}^{\infty} \left(-m/R\right) b_m\left(z^{m+1}\right), \tag{38}$$

from which the result follows.

The following will be useful for comparing asymptotic bounds.

Definition 1. Let $\{d_m\}$ be a series of real or complex numbers. Given a pair of real numbers (K, p) with $K, p \ge 0$, we will call (K, p) a bounding pair for $\{d_m\}$ if there exists an M > 0 such that

$$|d_n|n^p \leqslant K$$
 for all $n > M$. (39)

Observation 1. If K' > K, p' < p, and (K, p) is a bounding pair, then so is both (K', p) and (K, p').

We assume for the remainder of this appendix that $\varinjlim d_m = 0$ (this is a necessary condition for convergence). The sequence of coefficients $S := \{d_m\}$ is said to have *polynomially bounded decay* if there exists p' > 0 for which the set of bounding pairs (K,p') is empty (i.e. the sequence $\{d_m m^{p'}\}$ is unbounded). If, in addition, there exists a bounding pair (K,p'') for this sequence with p'' > 0, we say that S has *polynomial decay*, with decay rate lying in the interval [p'',p'].

Observation 2. The set

$$I := \{ p \mid \{ d_m m^p \} \text{ is unbounded} \} \tag{40}$$

is a subinterval of $[0, \infty)$.

As I is a non-empty subset of $[0, \infty)$, it is bounded below and therefore has a greatest lower bound (glb). The interval I, and therefore also its glb, obviously depend on the sequence of coefficients S.

For each non-empty I = I(S), we will write k = k(S) for the glb of I(S). The sequence S will have polynomial decay iff k(S) > 0; in this case we refer to k(S) as the polynomial decay rate of S. In what follows we will only be concerned with sequences S having polynomial decay.

The glb k(S) may or may not be contained in I(S). We will assume that I(S) is non-empty and $k(S) \notin I(S)$. Define $J(S) = [0, \infty) - I(S)$ as the complement of I(S) in $[0, \infty)$.

Observation 3. For I(S) non-empty J(S) = [0, k(S)].

Let A_0 denote the radial line through the tip of the (unique) tallest mountain, and A_{π} the colinear radial line in the opposite direction. For the polyhedral planet defined above in section 7.2, k(S) = 7/2 and J(S) = [0,7/2] for all radial lines A distinct from A_0 and A_{π} , where S denotes the coefficients of the TS (35). Moreover, for the radial line A_{π} k(S) = 3 and J(S) = [0,3]. So the assumptions made above on I(S) and k(S) hold for all radial lines except A_0 .

Fix a radial line *A* where J(S) = [0,k]. By definition the sequence $S = \{b_m m^k\}$ is bounded. Fix N > 0. We say M > 0 is an *N-bound* for *S* if $|b_m m^k| \le M$ for all $m \ge N$.

$$Bd(S,N) := \{M > 0 \mid M \text{ is an } N - \text{ bound for } S\}. \tag{41}$$

The following is clear.

Proposition 3. For each N > 0 Bd(S,N) is an interval in $(0,\infty)$. Moreover if 0 < N < N' then $Bd(S,N) \subset Bd(S,N')$.

Let

$$Bd(S,\infty) = \varinjlim_{N} Bd(S,N). \tag{42}$$

By the above proposition this is a direct limit of intervals in $(0,\infty)$, hence also an interval. Let K(S) be the glb of $Bd(S,\infty)$. We call S stable if $K(S) \in Bd(S,\infty)$. In that case $Bd(S,\infty) = [K(S),\infty)$. Note that this also implies K(S) > 0.

Theorem 2. Let $A \neq A_0$ denote a radial line other than A_0 , $S_V = \{b_m\}$ the set of Taylor series coefficients for $TS(V^A)(z)$ (as in (35)), and $S_{g_r} = \{c_m\}$ the set of Taylor series coefficients for g_r^A (as in (36)). Then both S_V and S_{g_r} are stable. Moreover $k(S_{g_r}) = k(S_V) - 1$ and

$$\frac{K(S_V)}{K(S_{g_r})} = R. (43)$$

Proof. The stability of both S_V and S_{g_r} follows from the results of appendix A when $A \neq A_{0,\pi}$. And for $A = A_{\pi}$ it can be verified by direct inspection.

Suppose (p, M) is a bounding pair for S_V ; this means there exists N > 0 such that $|b_m m^p| < M$ for $m \ge N$. Fixing $\varepsilon > 0$, we may choose N' > N so that $|b_m (m+1)^p| < M + \varepsilon$ for all $m \ge N'$. By proposition 2 when m > N' we have

$$|c_{m+1}(m+1)^{p-1}| = \frac{1}{R} |(m+1)b_m(m+1)^{p-1}|$$

$$= \frac{1}{R} |b_m(m+1)^p| < \frac{M+\varepsilon}{R}, \qquad (44)$$

implying $(p-1,(M+\varepsilon)/R)$ is a bounding pair for S_{g_r} . The same analysis applies in the other direction, showing that if (q,M') is a bounding pair for S_{g_r} then (q+1,R*M') is a bounding pair for S_V . This implies both that $k(S_{g_r}) = k(S_V) - 1$ and $K(S_{g_r}) = K(S_V)/R$.

Let PS_V denote the sequence of partial sums error for the TS in (35), and PS_{g_r} the sequence of partial sums error for the TS in (36).

Theorem 3. Let $A \neq A_0$ denote radial line other than A_0 . Then both PS_V and PS_{g_r} have polynomial decay and are stable. Denote the polynomial decay rates respectively by $b(PS_V)$ and $b(PS_{g_r})$. Then $b(PS_V) = k(S_V)$, $b(PS_{g_r}) = k(S_{g_r})$. Also denote by $B(S_V)$ and $B(S_{g_r})$ the glbs of $Bd(PS_V, \infty)$ and $Bd(PS_{g_r}, \infty)$ respectively. Then

$$\frac{B(S_V)}{B(S_{g_r})} = R. \tag{45}$$

Proof. The equalities $b(PS_v) = k(S_V)$ and $b(PS_{g_r}) = k(S_{g_r})$ follow from the fact that the series S_V and S_{g_r} are sufficiently alternating when $A \neq A_0$. Let α represent the angle formed by A_0 and A (note that $\alpha > 0$ as $A \neq A_0$). By the results of appendix A, we have

$$B(S_V) = K(S_V)/(2\sin(\alpha/2)),$$

$$B(S_{g_r}) = K(S_{g_r})/(2\sin(\alpha/2)).$$
 (46)

Then

$$\frac{B(S_V)}{B(S_{\sigma_o})} = \frac{K(S_V)}{K(S_{\sigma_o})} = R \tag{47}$$

by theorem 2.

In the notation of the main text of this paper, we have shown that for any radial line other than the singular radial line

$$\frac{B^V}{B^g} = \frac{K^V}{K^g} = R. \tag{48}$$

ORCID iD

M Bevis https://orcid.org/0000-0002-4944-8186

References

Bothwell T, Kennedy K and Aeppli A 2022 Resolving the gravitational redshift across a millimetre-scale atomic sample *Nature* **602** 420–7

Bucha B, Hirt C and Kuhn M 2019 Cap integration in spectral gravity forward modelling up to the full gravity tensor *J. Geodesy* **93** 1707–37

- Costin C, Costin R, Ogle C and Bevis M 2022 On the domain of convergence of spherical harmonic expansions *Commun. Math. Phys.* 389 875–97
- Ecker E 1972 On the spatial convergence of spherical harmonic series Translation from German, DMAAC-TC-1849, St Louis, MO
- Fukushima T 2020 Taylor series expansion of prismatic gravitational field *Geophys. J. Int.* **220** 610–60
- Guo J 2023 Physical Geodesy: A Theoretical Introduction (Springer) p 501
- Heiskanen W and Moritz H 1967 *Physical Geodesy* (W.H. Freeman and Company) 1979 corrected reprint
- Hirt C and Kuhn M 2017 Convergence and divergence in spherical harmonic series of the gravitational field generated by high resolution planetary topography-a case study for the Moon *J. Geophys. Res. Planets* 122 1727–46
- Hofmann-Wellenhof B and Moritz H 2006 *Physical Geodesy* (Springer) 2nd corrected edn
- Hu X and Jekeli C 2015 A numerical comparison of spherical, spheroidal and ellipsoidal harmonic gravitational field models for small nonspherical bodies: examples for the Martian moons J. Geod. 89 159–77
- Jekeli C 1983 A numerical study of divergence of spherical harmonic series of the gravity and height anomalies at the Earth's surface *Bull. Geod.* **57** 10–28
- Jekeli C 1988 The exact transformation between ellipsoidal and spherical harmonic expansions *Manuscr. Geod.* 13 106–13
- Kellogg O 1929 Foundations of Potential Theory (Verlag Von Julius Springer) p 384
- Kholshevnikov C 1977 On convergence of an asymmetrical body potential expansion in spherical harmonics *Celest. Mech.* **16** 45–60
- Krarup T 1969 A Contribution to the Mathematical Foundation of Physical Geodesy vol 44 (Danish Geodetic Institute)

- Lowes F J and Winch D E 2012 Orthogonality of harmonic potentials and fields in spheroidal and ellipsoidal coordinates: application to geomagnetism and geodesy *Geophys. J. Int.* 191 491–507
- McGrew W F *et al* 2018 Atomic clock performance enabling geodesy below the centimetre level *Nature* **564** 87–90
- Moritz H 1961 Über die konvergenz der kugelfunktionsentwicklung für das außenraumpotential an der erdoberfläche *Österr. Z. Vermess.* **49** 11–15
- Moritz H 1980 Advanced Physical Geodesy 2nd edn (Wichmann) Reprinted from the 1st edn
- Ogle C, Costin O and Bevis M 2021 Non-convergence of spherical harmonic expansions below the Brillouin sphere—the continuous case *J. Math. Phys.* **62** 102901
- Pavlis N, Holmes S, Kenyon S and Factor J 2012 The development and evaluation of the Earth Gravitational Model 2008 (EGM2008) *J. Geophys. Res.* 117 1–38
- Sansò F and Sideris M 2013 Geoid Determination: Theory and Methods (Springer) p 734
- Sjöberg L E 1980 On the convergence problem for the spherical harmonic expansion of the geopotential at the surface of the earth *Boll. Geod. Sci. Affini* **39** 261–70
- Šprlák M and Han S 2021 On the use of spherical harmonic series inside the minimum Brillouin sphere: theoretical review and evaluation by GRAIL and LOLA satellite data *Earth Sci. Rev.* 222 103739
- Tegmark M 1996 An icosahedron-based method for pixelizing the celestial sphere *Astrophys. J.* **470** L81–L84
- Wang Y M 1997 On the error of analytical downward continuation of the Earth's external gravity potential on and inside the Earth's surface *J. Geodyn.* **71** 70–82
- Werner R A 1994 The gravitational potential of a homogeneous polyhedron, or, don't cut corners *Celest. Mech. Dyn. Astron.* **59** 253–78